Available online at www.sciencedirect.com

ScienceDirect

Advances in Space Research 77 (2026) 10947–10971

ADVANCES IN SPACE RESEARCH (a COSPAR publication)

www.elsevier.com/locate/asr

Modelling future launch traffic and the associated risk to new missions ☆

Callum Wilson [a], Massimiliano Vasile [a,*], Jinglang Feng [a], Keiran McNally [b], Nina Maric [b], Andre Horstmann [c]

[a] Department of Mechanical and Aerospace Engineering, University of Strathclyde, 75 Montrose Street, Glasgow G1 1XJ, United Kingdom
[b] GMV, Airspeed 2 Eight Street, Harwell, Oxfordshire OX11 0RL, United Kingdom
[c] ESA/ESOC - European Space Operations Centre, Robert-Bosch-Str. 5, Darmstadt 64293, Germany

Received 1 February 2025; received in revised form 27 June 2025; accepted 21 July 2025
Available online 25 July 2025

Abstract

Due to the recent increase in the rate of launches to space, there is a renewed interest in modelling the evolution of the space environment. These models aim to predict how objects, including active spacecraft and debris, will be distributed in the environment in future. This work focusses on two components of an overall environment model: the launch traffic model and the risk model. Many space environment models that require an estimate of launch traffic will either use no launches as a baseline or repeat historical data. Recent shifts in launch traffic have shown that this approach is unrealistic and does not account for potential further changes in launch traffic. Models of risk in the space environment aim to quantify the risk posed to a mission by other objects in the environment and the additional risk a new mission generates to other objects in the environment as a result of potential collisions. This is difficult to calculate over the lifetime of a mission due to the number of encounters and the uncertainty in how active satellites are distributed in the environment. Our proposed approach to modelling launch traffic is a parametric model that can simulate various future launch scenarios. This model calculates the total number of objects launched per year using an exponential-logistic curve to capture the sharp increase in launch traffic. To determine the location and physical characteristics of launched objects, the model fits probability distributions to data from previous launches. These distributions can vary over time to simulate other changes in launch trends aside from the number of objects. The launch traffic model can be used along with other debris environment modelling tools to simulate the evolution of the space environment and accordingly to calculate the risk of collision for new missions. Our proposed model of risk estimates the likelihood and severity separately, where risk likelihood is a measure of the probability of collision and severity quantifies the consequences of a collision. The likelihood estimate comes from the intersection of distributions of orbital parameters, which is suitably fast to calculate over the lifetime of a mission. The model of severity in the environment uses a simple model to approximate the effects of a collision without needing to propagate all fragments. In addition, we model the severity of collisions for the mission of interest based on the predicted effect of a collision on the spacecraft. This work used different launch scenarios to generate varying evolutions of the space environment. Results are shown from applying the risk model to example missions across these scenarios.
© 2025 The Authors. Published by Elsevier B.V. on behalf of COSPAR. This is an open access article under the CC BY-NC-ND license (http://creativecommons.org/licenses/by-nc-nd/4.0/).

Keywords: Space environment; Launch traffic; Collision risk

1. Introduction

Launch traffic from commercial operators has increased dramatically in recent years and brought about a new era in the space industry that is commonly referred to as "NewSpace". There are now more artificial satellites in

☆ This article is part of a special issue entitled: 'Space Sustainability' published in Advances in Space Research.

* Corresponding author.
E-mail address: massimiliano.vasile@strath.ac.uk (M. Vasile).

https://doi.org/10.1016/j.asr.2025.07.055
0273-1177/© 2025 The Authors. Published by Elsevier B.V. on behalf of COSPAR.
This is an open access article under the CC BY-NC-ND license (http://creativecommons.org/licenses/by-nc-nd/4.0/).

Nomenclature

ADR	Active Debris Removal
BLE	Ballistic Limit Equation
CDF	Cumulative Distribution Function
ECOB	Environmental Consequences of Orbital Break-ups
GEO	Geostationary Earth Orbit
GMM	Gaussian Mixture Model
KS	Kolmogorov–Smirnov
LEO	Low Earth Orbit
MEO	Medium Earth Orbit
MMOD	Micro-Meteoroids and Orbital Debris
MOID	Minimum Orbit Intersection Distance
NSO	Navigation Satellite Orbit
PDF	Probability Density Function
PMD	Post Mission Disposal
RSO	Resident Space Object
SBM	Standard Breakup Model
SMA	Semi-Major Axis

orbit than ever before which pose a risk to other objects in the environment (ESA Space Debris Office, 2025). This is a result of the increased availability of commercial launches, which has enabled many more entities to launch satellites and has seen the beginning of several large satellite constellations. The growth of the space sector has many benefits, including increased democratisation of access to space and a greater number of available space services. However, it has also resulted in far more traffic from active payloads (Diserens et al., 2020). Although the long-term effects of this change in the environment remain unknown, there are already several consequences for space operations. One of these is that it is now more difficult to determine the risk of collisions for a given mission since there are so many objects, both active and inactive, to consider. This has implications for operators, who wish to minimise the risk to their mission; insurers, who must quantify the risk of a mission to insure it properly; and governing bodies, who are interested in ensuring the short- and long-term safety of the space environment.

The issue of increased traffic in space has motivated more research into models of the space environment. Such models aim to capture future trends in the number and location of objects in space – including active payloads and debris. Most space agencies have published software for this purpose, which include the LEGEND simulator from NASA (Liou et al., 2004), DELTA from ESA (Virgili, 2016), MEDEE from CNES (Dolado-Perez et al., 2013), SOLEM from CNSA (Wang and Liu, 2019), and NEODEEM from JAXA (Narumi et al., 2008). One significant source of uncertainty in all of these models is launch traffic. This refers to the number of objects added to the space environment via launches. The number of objects launched in future will depend on several factors that are difficult to predict, such as availability and cost of launches or demand for new missions.

Most existing approaches to modelling space traffic repeat historical launches into the future. This is the case in published analyses of MEDEE (Dolado-Perez et al., 2013), NASA's ORDEM software (Matney et al., 2019) and SOLEM (Wang and Liu, 2019), which all use 8 years of launch data repeated over several decades. This approach of repeating historical launches fails to account for the sharp increase in traffic seen since 2019 that is largely due to Starlink launches. Other models might include theoretical constellations as separate from other launches, which when considered separately follow a more predictable trend (Martin et al., 2004; Kawamoto et al., 2018). In the study of Kawamoto et al. on debris mitigation measures, the authors include a theoretical mega-constellation of 1000 satellites. This is still fewer than the current number of Starlink satellites in orbit, which highlights the difficulty of estimating the number of additional objects resulting from future launches.

Other than directly repeating historical launch data, some studies extrapolate the number of launches from existing data (Lucken and Giolito, 2019; Lewis et al., 2014). In the study of Lewis et al. (2014), which focusses on the risk associated with CubeSats, the baseline launch model repeats data from 2005 to 2012. The number of CubeSats launched each year were modelled with a logistic function in time. A similar later study on the impacts of small satellite launches used the same logistic function for monitoring total number of CubeSats launched (Radtke et al., 2017). Instead of drawing orbital parameters directly from past launches, these were sampled from a Gaussian Mixture Model (GMM) fit to data from previous launches.

The launch traffic models described above do not consider the state of the space environment at the time of launch. However, increasing collision risk in certain crowded orbits will likely result in fewer launches to these regions. Moreover, potential changes in policies regarding space traffic could cause changes to launch patterns. An alternative model of launch traffic proposed in Rao and Letizia (2021) aims to incorporate these factors into its predictions using an econometric model. This approach is similar to models of consumer behaviour that are used in many other applications and allows forecasting of the space environment under different assumptions of future policy choices and market conditions.

As a result of the increased number of objects in the space environment, there is now an increased rate of potential in-orbit collisions between objects. The problem of estimating the probability of collision for individual encounters

is very well studied (Alfano and Oltrogge, 2018). However, this can be difficult to extend to the lifetime of a mission due to the number of potential encounters. There are also several existing methods for analysing long term probabilities of collision between all Resident Space Objects (RSOs). One class of approaches applies orbit filters to screen pairs of objects that will not collide and calculates collision probabilities between the remaining objects (Woodburn et al., 2010). This is only applicable to tracked objects and still requires many computations of collision probability for individual pairs of objects. Other approaches such as CUBE (Liou et al., 2003) take a more statistical view of the environment to estimate collision probability. In this formulation, the environment is divided into discrete control volumes and collisions can only occur between objects located within the same volume. Debris environment models such as ORDEM and ESA's MASTER can calculate the debris flux rate for a given orbit (Horstmann et al., 2021), which also model the environment in a statistical manner. The approaches described above consider only the likelihood of a collision, but not the resulting effect on the environment. Many "debris indices" have been proposed to quantify the risk associated with an object, which considers both the likelihood and effect of collisions (McKnight et al., 2021). These indices aim to find which inactive objects pose the most danger to the environment. Several of these indices are "risk-based" metrics that consist of the product of likelihood and severity.

In this work, we propose a new parametric model of future launches that better captures recent trends in the number of objects launched. This model leverages historical launch data to estimate characteristics of future launches and can adjust the launch rate based on qualitative assumptions on future trends. The proposed model takes a similar approach to the CubeSat launch model of Radtke et al. (2017) extended to all classes of object launches. Another aspect of this model that is different to previous methods of predicting launches is the ability to vary the physical and orbital characteristics of launched objects over time. This is necessary to allow for changing demand in different orbital regions or the types of payloads launched, as has been observed in the past.

One potential application of this launch model is for predicting the risk of collision for future missions based on the evolution of the environment. Measures of risk are determined by the likelihood and outcome of an event. The likelihood in this case is the probability of a collision and the outcome, or severity, has two parts: induced and encountered severity. Induced severity quantifies the effect of a collision on other objects in the environment. Encountered severity quantifies the effect of a collision on the mission of interest. In addition to the launch model, a further contribution of this work is a novel approach to modelling induced and encountered risk that is suitably fast to be applied across the duration of a mission. This risk model incorporates the launch model to estimate the future population and induced consequences of collisions.

In the proposed model of collision risk, collision likelihood is estimated via the intersection of distributions of RSOs and the distribution of the mission of interest. Modelling the mission as a distribution allows this approach to scale well to multiple satellites in a single mission. The calculation of encountered severity accounts for untracked objects based on debris environment simulations. The proposed method for calculating induced risk aims to model the consequence of fragments from a collision without the need for simulating every fragmentation. The model of induced risk described here differs from other risk-based metrics primarily in its calculation of the likelihood, which uses a novel approach based on distributions of objects. Moreover, the estimation of consequences in this metric is dependent on the simulated future launch traffic, which is an aspect that is often not included in other metrics. While most risk based metrics focus on Low Earth Orbit (LEO), the proposed metric is demonstrated here across LEO, Medium Earth Orbit (MEO), and Geostationary Earth Orbit (GEO) orbital regions.

The remainder of this paper is organised as follows. Section 2 describes the proposed launch model and shows example outputs from each part of the model. Section 3 defines the risk model and the process for calculating collision likelihood, encountered severity, and induced severity. This model requires the definition of several parameters that are calculated in Section 4. Section 5 describes the launch model scenarios used in simulating different evolutions of the space environment. Results are shown from applying the risk model to example missions in each of these scenarios in Section 6.

2. Launch traffic model

The proposed launch traffic model has the following steps:

1. Calculate the trend in total number of objects launched per year,
2. Determine the proportion of each object class (payloads, rocket bodies, mission related objects) based on historical data,
3. For each object class, sample orbital and physical parameters from a distribution fit to historical data,
4. (Optionally) define time-varying weights for each distribution to account for changes in orbital and physical characteristics over time.

Each of these steps takes into account historical launches and has parameters that can be adjusted depending on predicted future launch behaviour. The following sections give further details on each part of the model.

2.1. Total launch trend

The launch traffic considered in this model consists of all payloads and other objects left in orbit as a result of

launches. In the first step of the launch traffic model, we estimate the total number of objects launched per year. The goal of this part of the model is to have a parametric representation of the number of objects launched that can capture any large increases in launch traffic and simulate a range of potential scenarios. To achieve this, we express the total number of objects launched each year as a sum of logistic-exponential curves. The logistic curves can represent sudden increases in launch traffic similar to that observed in recent years, while the exponential curves account for general increases in launch traffic over time. Summing multiple curves allows the model to simulate further large increases in launch traffic in future. The general form of this trend is

$$N(t) = n_0 + \sum_{i=1}^{M} \frac{A_i \cdot \exp(d_i(t - t_{0i}))}{b_i + \exp(-c_i(t - t_{0i}))}, \quad (1)$$

where N is the total number of objects launched in year t and M is the number of individual logistic-exponential curves that define the overall trend. The parameters $(n_0, A_i, b_i, c_i, d_i, t_{0i})$, $i = 1, 2, \ldots, M$ can be adjusted to create different forecasts. The analyses that follow only consider the simplest case of a single logistic-exponential curve such that $M = 1$.

The trend presented above is suitably flexible to model a variety of scenarios, but as a result requires definition of at least 6 parameters. In some cases, particularly outside of LEO, a simpler model might be desired and sufficient to capture general trends in the number of objects launched. For this reason, we also define a linear trend which has the form

$$N(t) = n_0 + A(t - t_0), \quad (2)$$

where in this case n_0 is the number of objects launched in year $t = t_0$ and A is the gradient.

Figs. 1–4 show the effect of each parameter on the logistic-exponential trend of Eq. 1. t_0 is the time of the inflection point in the curve and n_0 is the initial value of N at a time $t \ll t_0$ as shown in Fig. 1. Fig. 2 shows the effect of varying A and b, which both control the magnitude of increase in N, but can result in different curve shapes as shown in the figures. Increasing A or decreasing b results in a larger number of objects launched in the future.

The parameter c controls the rate at which N increases as shown in Fig. 3. Higher values of c result in a steeper rate of increase in the number of objects launched. Fig. 4 shows the effect of varying d, which controls the rate of increase in N where $t > t_0$. When $d = 0$, the number of objects launched reaches a plateau some time after t_0. Increasing d instead results in a further exponential increase in the number of objects launched after t_0.

The launch model defines separate trends in the number of objects launched for LEO, MEO, and GEO. In the following examples, we demonstrate how the launch model can generate a range of future scenarios in terms of how many objects will be launched. The model parameters in

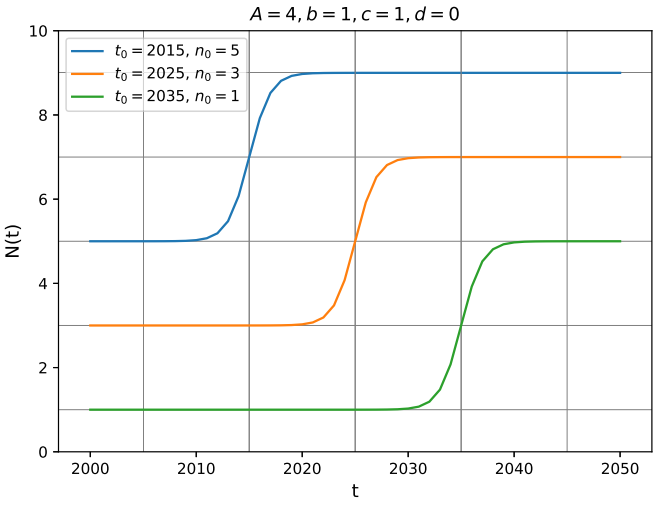

Fig. 1. Effect of t0, n0.

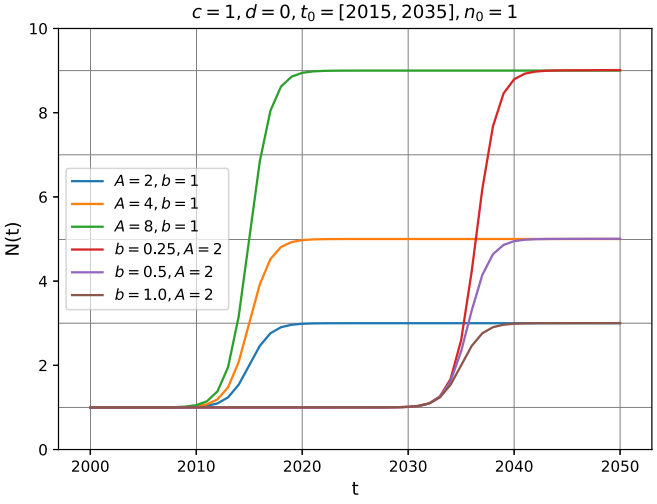

Fig. 2. Effect of A, b.

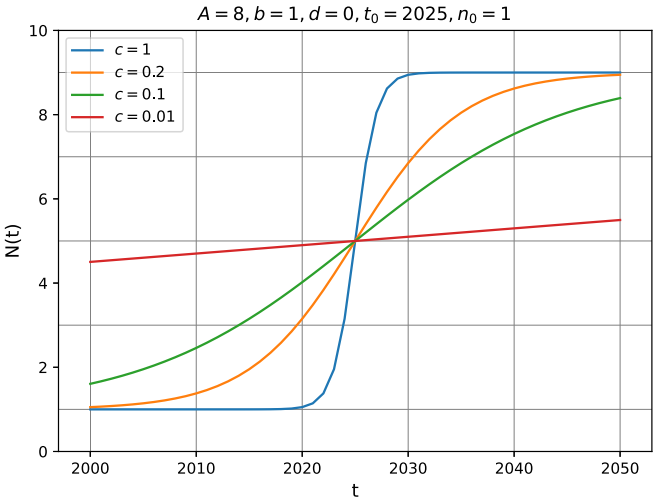

Fig. 3. Effect of c.

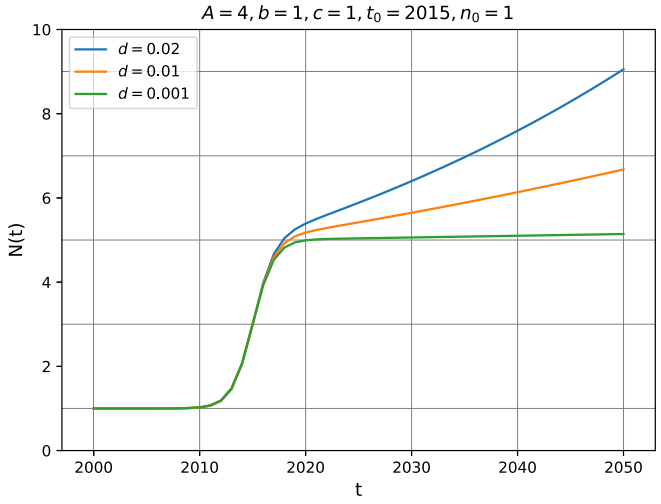

Fig. 4. Effect of d.

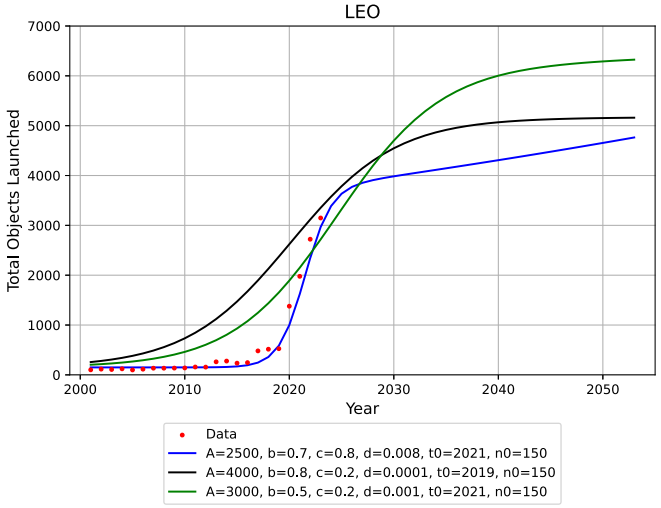

Fig. 5. Number of objects launched to LEO from 2001–2023 with different forecasts shown.

these examples were chosen to loosely follow the trend of historical launches, but give qualitatively different future trends, e.g. a steady increase or plateau in rates of object launches. Fig. 5 shows three different forecasts using this model for the number of objects launched to LEO between 2024 and 2053. The data shown on the graph for previous years come from DISCOSWeb [1]. These are the total number of individual payloads, rocket bodies, and mission related objects launched each year. The blue curve shows a scenario where the number of objects launched does not continue to increase as rapidly as it has since 2019 and only gradually increases over the next 30 years. The green and black curves give alternative scenarios where the launch rate continues to increase more steadily in the future.

The data shown in Fig. 5 include all constellation payloads, which constitute the majority of recent launch traffic. These payloads can also be considered separately from other launched objects and added based on proposed or approved launch plans. There are several different sources that detail these planned constellations. For example, the LEO Satcom Report from Prime Movers Lab, which lists over 200,000 satellites as parts of large constellations (Stein, 2022) and a report from the MITRE corporation that lists over 136,000 planned constellation satellites (Long, 2020). Fig. 6 shows some example launch trends fit to historical launch numbers excluding constellations. While the number of objects launched each year is significantly lower, there is still an increase over the past few years that is captured by the model.

Although the launch trends in MEO and GEO have not seen the same sharp increase as in LEO, this parametric model of launches is also applicable in these regimes. Depending on the assumptions made, it may be suitable to use the linear trend of Eq. 2 or have a trend that decreases over time. Examples of these trends for MEO

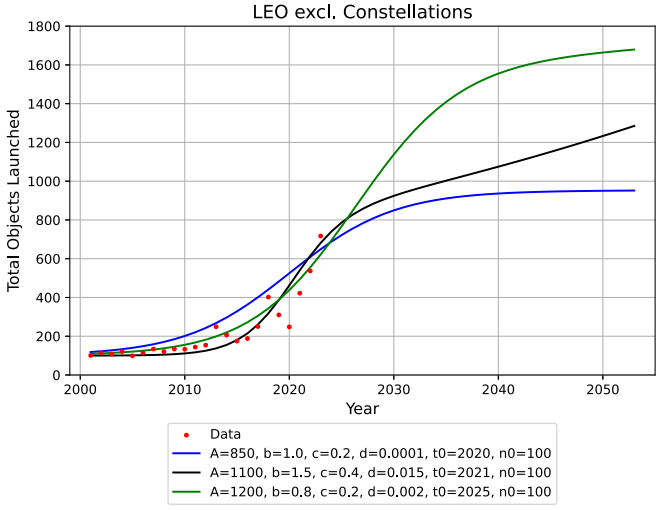

Fig. 6. Number of objects excluding constellation payloads launched to LEO from 2001–2023 with different forecasts shown.

and GEO are shown in Figs. 7 and 8. Data shown in both plots include all constellation payloads since they make up a far lower proportion of overall traffic compared to LEO.

The blue log-exponential curve in Fig. 7 for MEO assumes a steep increase in traffic to this region followed by a more gradual increase from 2040 onwards. The other examples in MEO use a simpler linear trend and show a gradual increase or no increase at all in launch traffic to this region. Similarly, in Fig. 8 the blue curve shows a relatively steep increase followed by a plateau. It is also possible to model a decrease in launch traffic with appropriate choice of parameters, as shown in the green curve.

2.2. Proportions of object classes

Another consequence of the recent changes in launch traffic is a change in the proportions of each object class being launched. This model considers three different classes

[1] https://discosweb.esoc.esa.int/

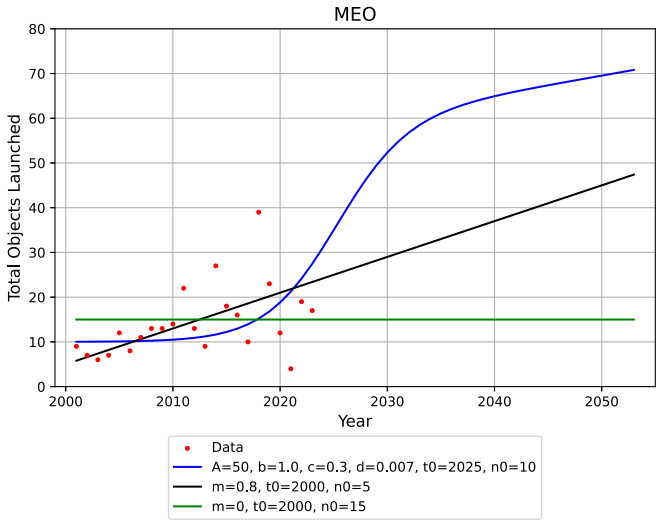

Fig. 7. Number of objects launched to MEO from 2001–2023 with different forecasts shown.

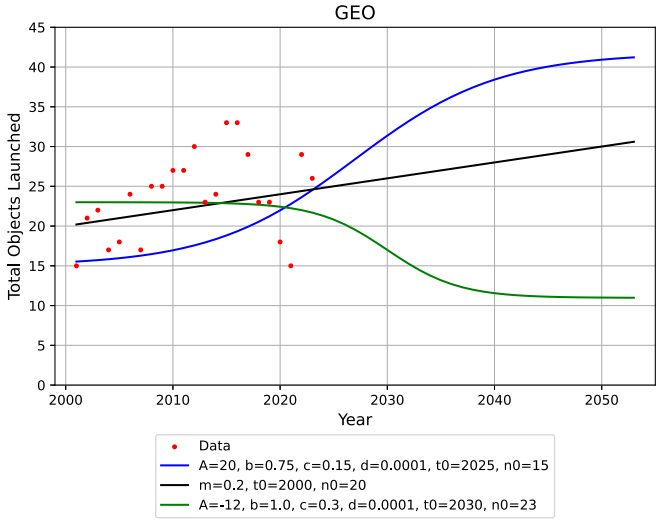

Fig. 8. Number of objects launched to GEO from 2001–2023 with different forecasts shown.

of launched objects: payloads, rocket bodies, and mission related objects, which are defined in the ESA Space Environment Report (ESA Space Debris Office, 2025). Individual launches can now contain many payloads and it is common to have smaller satellites "piggyback" on launches for larger missions. This is highlighted in Fig. 9, which shows the proportion of payloads, rocket bodies, and mission related objects launched to LEO since 2014. Payloads clearly take up a far greater share of object launches, which must be accounted for in launch forecasts. An additional set of parameters that can be controlled in this launch model is the proportion of object classes launched in a given year, with the potential to increase or decrease the relative number of each object per launch. The distribution of object classes also changes substantially when excluding

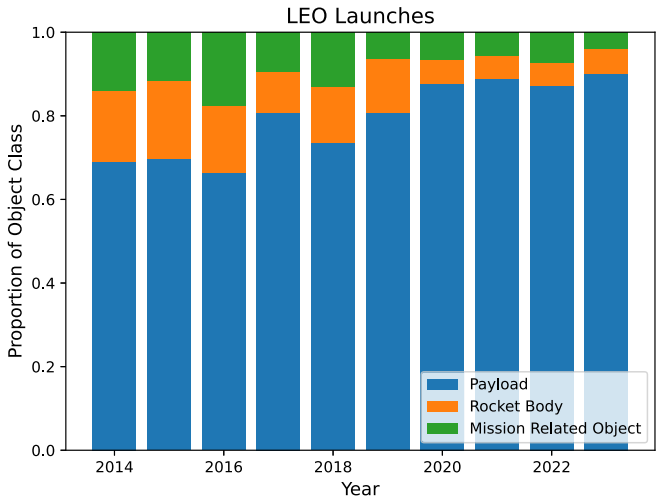

Fig. 9. Proportion of each object class launched to LEO for the previous ten years.

constellations as shown in Fig. 10. Constellation launches tend to have more payload objects per launched rocket and so excluding constellations results in a greater share of rocket bodies in total launched objects.

As with the number of objects launched, MEO and GEO see less variation in the proportion of each object class in recent years as shown in Fig. 11 and Fig. 12. In MEO, there have been very few mission related objects launched to this region but a large number of rocket bodies relative to the total number of launched objects. In GEO, rocket bodies and mission related objects are much more rare.

2.3. Distributions of orbital and physical parameters

In addition to the number of objects launched, it is necessary to model the orbits into which objects are launched since certain regions experience higher traffic than others. Furthermore, to predict the evolution of objects' orbits and their associated risk it is useful to model their physical properties. This is achieved by fitting a distribution to previous object launches with separate models defined for each object class and orbit regime. The distribution of orbital parameters models the Semi-Major Axis (SMA), eccentricity, and inclination of previous launches. In LEO and MEO, the RAAN, argument of pericentre, and mean anomaly are assumed uniformly distributed across objects. The distribution of launches to GEO can also include the RAAN and argument of pericentre. A separate distribution for the physical parameters models the cross-sectional area, mass, and characteristic length of each object class. In the case of these parameters, the fit is to the log values of each due to the large range of values for each parameter. Moreover, due to the physical relationships between each of these parameters, on a log scale their relationship is approximately linear which is useful for fitting the distributions.

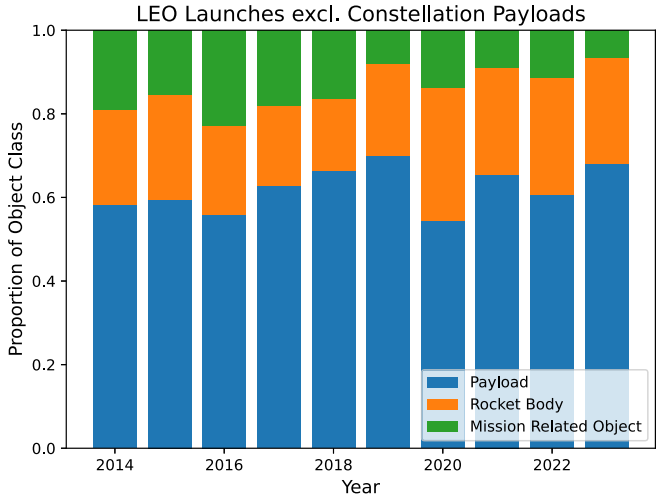

Fig. 10. Proportion of each object class launched to LEO for the previous ten years excluding constellation payloads.

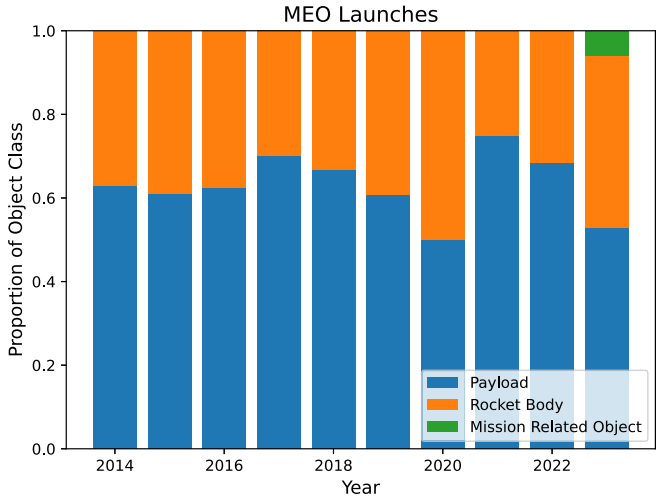

Fig. 11. Proportion of each object class launched to MEO for the previous ten years.

The distribution used here is a Gaussian Mixture Model (GMM), which has a Probability Density Function (PDF) of the form

$$p(\mathbf{x}) = \sum_{i=1}^{K} w_i \varphi(\mathbf{x}|\boldsymbol{\mu}_i, \boldsymbol{\Sigma}_i), \tag{3}$$

where $\mathbf{x}$ is the vector of parameters to be modelled, K is the number of components, φ is the PDF of a multivariate normal distribution with means $\boldsymbol{\mu}$ and covariance $\boldsymbol{\Sigma}$, and w_i is the weight of the i^{th} component. This distribution models the orbital and physical characteristics of previous object launches. When simulating future launch scenarios, objects are sampled from these distributions to obtain their relevant parameters.

Figs. 13 and 14 show examples of the historical launch data and samples from distributions fit to those data points. In Fig. 13 this is done for the area, mass, and length

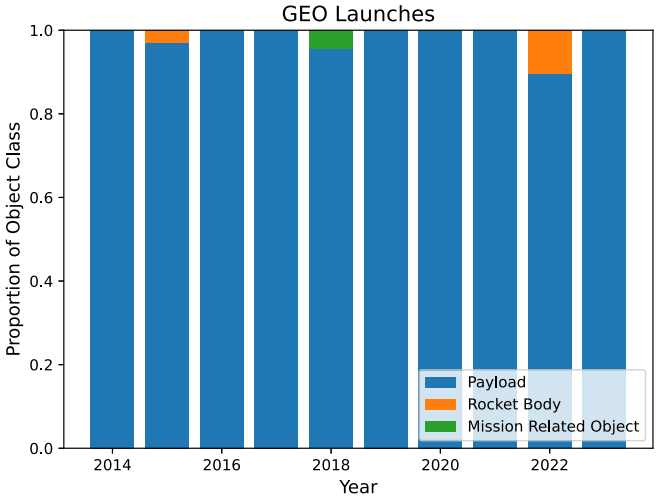

Fig. 12. Proportion of each object class launched to GEO for the previous ten years.

of payloads, excluding constellation payloads, launched to LEO between 2016 and 2023. The distribution is a 10 component GMM fit using expectation maximisation. Similarly, Fig. 14 shows the SMA, eccentricity, and inclination of rocket bodies launched to LEO over the same time period fit to a 8 component GMM. To assess the model fit quantitatively, we use a multivariate extension of the KS test (Naaman, 2021). For a two sample multivariate KS test, the test statistic for the example payload physical parameter samples was 0.201 and for rocket body orbital parameter samples was 0.223. Using a significance level of $\alpha = 0.05$, in both cases we cannot reject the null hypothesis that the model samples and true values are from the same distribution. These examples show that the distribution samples successfully approximate the true distribution of launched objects.

2.4. Time-varying distributions

The steps described previously capture the distributions of orbital and physical parameters for previous launches. However, this does not account for potential changes in these distributions, such as having more launches to certain regions or changing object sizes. To capture such changes, as an optional additional step in the launch traffic model, the weights of the GMMs used to model physical and orbital parameters can be controlled with time-varying values. The choice of function to vary these weights is arbitrary; here we use the same logistic-exponential curve as in Eq. 1. This function is suitable as the logistic term can effectively model a step increase of a single weight. The weights of individual components vary according to Eq. 1 and are then normalised such that their sum is 1 as shown:

$$W_i(t) = w_0 + \frac{A_i \cdot exp(d_i(t - t_{0i}))}{b_i + exp(-c_i(t - t_{0i}))}, \tag{4}$$

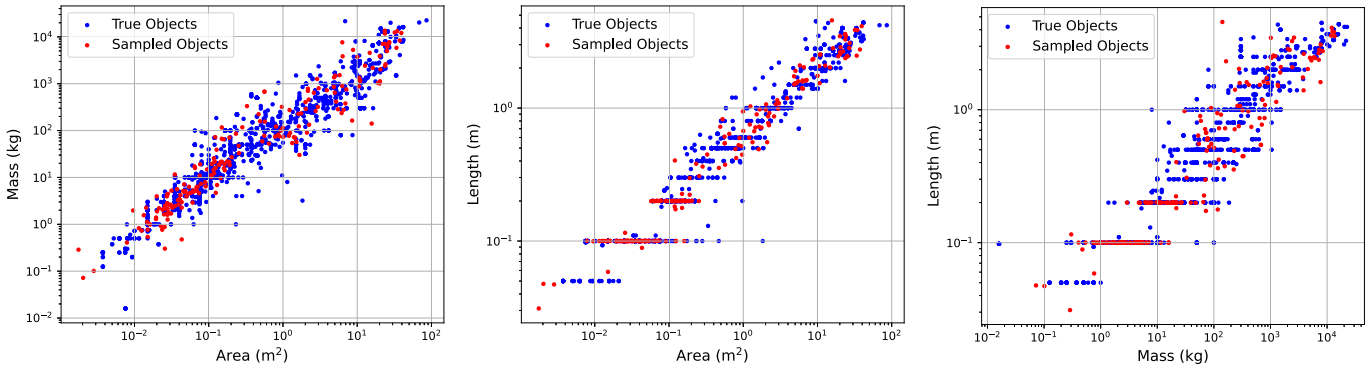

(a) Area-Mass (b) Area-Length (c) Mass-Length

Fig. 13. Physical parameters of payloads, excluding constellation payloads, launched to LEO and samples from a distribution fit to these data.

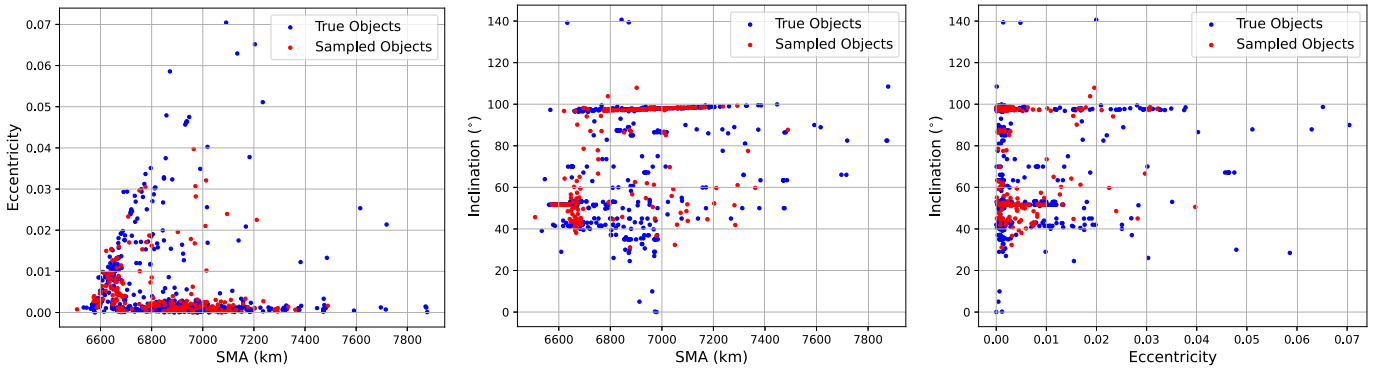

(a) SMA-Eccentricity (b) SMA-Inclination (c) Eccentricity-Inclination

Fig. 14. Orbital parameters of rocket bodies launched to LEO and samples from a distribution fit to these data.

$$w_i(t) = \frac{W_i(t)}{\sum_{j=1}^{K} W_j(t)}, \tag{5}$$

where w_{0i} is the initial value of the weight of the relevant component and the parameters A_i, b_i, c_i, d_i, and t_{0i} are selected for each component.

As with the model of the number of objects launched, controlling the weights in this manner gives a great deal of flexibility to a model user, but requires the definition of several parameters. In practice, these parameters can be chosen according to different qualitative assumptions on future trends. For example, in a GMM of physical parameters, each component represents groups of satellites of a similar size. Varying the weight of one of these components can increase or decrease the relative proportion of these satellites launched in future. In the case of orbital parameters, the components of a GMM fit to these parameters may not represent well-defined orbital regions. However, the weights of each component can still be varied to increase or decrease the proportion of objects in certain arbitrary regions of the relevant regime. This can also be used to alter the launch trend such that it fits with other forecasts for launches of specific classes of satellites, as demonstrated in previous work (Wilson et al., 2024). When fitting to other forecasts, this requires a degree of trial-and-error to find suitable parameters that match other trends well.

As an example of the time-varying weights, consider the 6 component GMM fit to only cross-sectional area and mass of payloads shown in Fig. 15. This figure shows the means of each component of the GMM. Varying the weight w_5 of this distribution according to Eq. (4) with $A = 0.3, b = 1, c = 2.5, d = 0, t_0 = 2025$, and $n_0 = w_5$ and then normalising each weight by Eq. (5) gives the trend shown in Fig. 16. Fig. 17 then shows how the associated probability density function of this model varies over 10 years, where the weight w_5 associated with the lowest mass and area increases and so the density of this component increases. This can be used to model different orbits or sizes of satellite becoming more or less frequently launched in future.

3. Risk model

Risk refers to the product of likelihood and severity. The likelihood is denoted l_{col} and is related to the probability of collision. The severity is denoted sf and is defined sep-

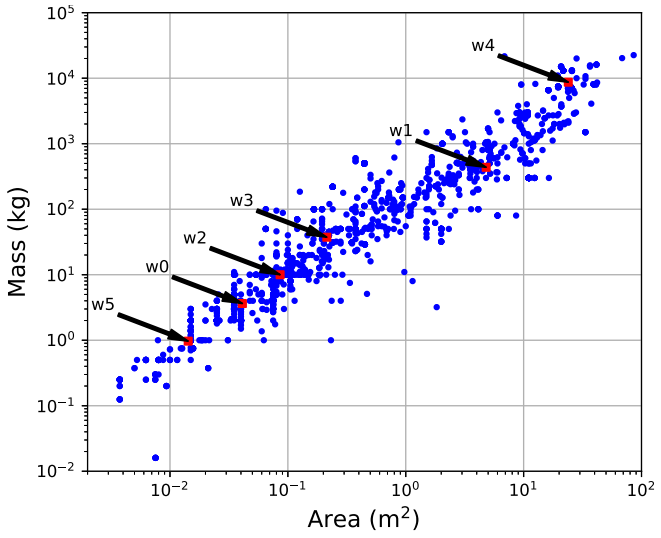

Fig. 15. Area and mass of previous payload launches and the means of a GMM fit.

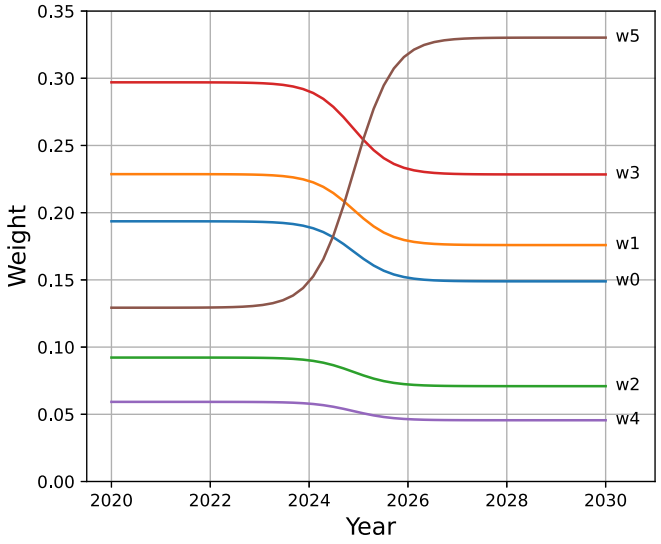

Fig. 16. Variation in GMM weights over time for area and mass of payloads.

arately for induced and encountered risk. The main steps of the proposed risk model are as follows:

1. Fit a GMM distribution of RSO and the mission of interest at different snapshots in time,
2. Estimate the collision likelihood at each snapshot by intersecting the two distributions via Minimum Orbit Intersection Distance (MOID) calculations,
3. Calculate the encountered severity factor based on the mass distribution of potential collisions,
4. Calculate the induced severity factor based on the estimated consequence of any debris produced by a collision.

3.1. Distributions of RSOs and single missions

The background population of RSOs is modelled as a probability distribution across the relevant orbital regime. This allows a fast estimation of collision likelihood without needing to know the exact position and covariance of every object. As with the distributions of launched objects, Gaussian Mixture Models (GMMs) are a suitable class of multivariate distributions for modelling the background population. These have a PDF as shown in Eq. (3).

In the distribution of RSOs, the parameters $\boldsymbol{x}$ are Keplerian orbital elements. In LEO and MEO, the RAAN and argument of pericentre are assumed to be uniformly distributed across the RSOs. Therefore, in these regimes the only parameters modelled in the GMM are SMA, eccentricity, and inclination. Objects in GEO have a stronger dependence on RAAN and argument of pericentre, so in this regime these parameters are included in the GMM. Fig. 18 shows the density of an example GMM fit to SMA, eccentricity, and inclination of RSOs in LEO over a single value of eccentricity. Higher density values in the plot indicate a higher likelihood of RSOs being present at those parameters.

Single missions can consist of a single satellite, fleet of multiple satellites, or a constellation of many satellites. In most cases, spacecraft that are part of a mission have a

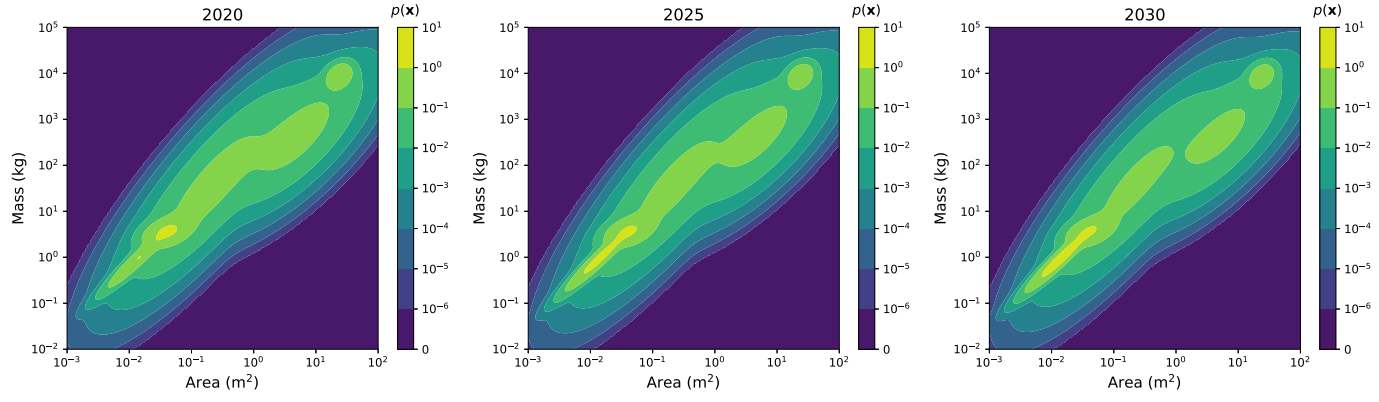

(a) 2020 (b) 2025 (c) 2030

Fig. 17. Variation in densities of payload area and mass over 10 years.

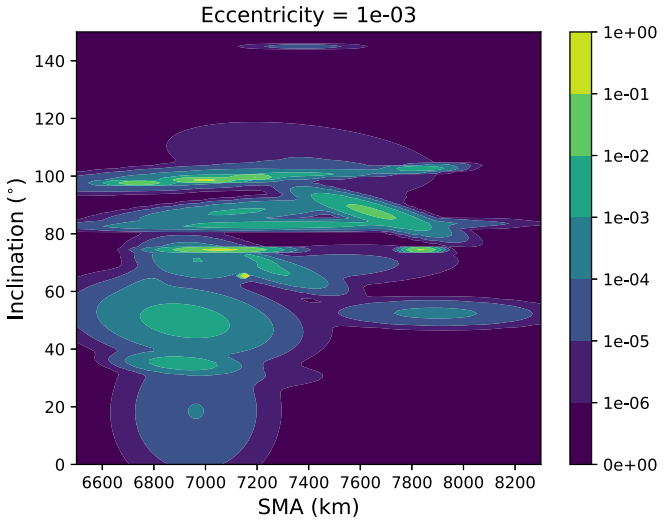

Fig. 18. Density of GMM fit to orbital parameters of the 2023 background population in LEO.

known orbit with small uncertainties. This means that the mission can be modelled as a single multivariate normal distribution at the location of each satellite. The variance of each normal distribution depends on the accuracy of satellite tracking. Large constellations that are located at a single altitude can also be modelled the same as a single satellite with the only difference being the number of satellites. As with the model of RSOs, the RAAN and argument of pericentre can be assumed uniformly distributed for a mission, except in GEO or specific orbits such as frozen orbits, where they are included in the distribution.

3.2. Collision likelihood via intersection of distributions

The collision likelihood between an object and RSOs is calculated from the intersection of their distributions. Instead of converting from orbital elements to covariances in cartesian coordinates, the proposed approach uses the Minimum Orbit Intersection Distance (MOID) between the distributions to approximate collision likelihood. Let X_{sat} and X_{bkgd} denote random variables representing the orbital parameters of the object of interest and RSOs respectively. These are distributed according to $p_{X_{sat}}(\mathbf{x}_{sat})$ and $p_{X_{bkgd}}(\mathbf{x}_{bkgd})$. The MOID is also a random variable that is a function of both sets of orbital parameters; i.e. $\text{MOID} = g(X_{sat}, X_{bkgd})$. The Cumulative Distribution Function (CDF) of the MOID is given by

$$\begin{aligned} F_{\text{MOID}}(v) &= P(\text{MOID} \leqslant v) \\ &= P(g(X_{sat}, X_{bkgd}) \leqslant v) \\ &= \int\int_D p_{X_{sat}X_{bkgd}}(\mathbf{x}_{sat}, \mathbf{x}_{bkgd}) d\mathbf{x}_{sat} d\mathbf{x}_{bkgd}, \end{aligned} \tag{6}$$

where $D = \{(\mathbf{x}_{sat}, \mathbf{x}_{bkgd}) | g(\mathbf{x}_{sat}, \mathbf{x}_{bkgd}) \leqslant v\}$, v is the value of the MOID, and $p_{X_{sat}X_{bkgd}}(\mathbf{x}_{sat}, \mathbf{x}_{bkgd})$ is the joint PDF of X_{sat} and X_{bkgd}. Since the orbital parameters of the object and the RSOs are independent, we can write that

$$p_{X_{sat}X_{bkgd}}(\mathbf{x}_{sat}, \mathbf{x}_{bkgd}) = p_{X_{sat}}(\mathbf{x}_{sat}) p_{X_{bkgd}}(\mathbf{x}_{bkgd}). \tag{7}$$

The probability that the MOID between the distributions is less than a threshold value of v can therefore be expressed as

$$P(\text{MOID} < v) = \int\int_D p_{X_{sat}}(\mathbf{x}_{sat}) p_{X_{bkgd}}(\mathbf{x}_{bkgd}) d\mathbf{x}_{sat} d\mathbf{x}_{bkgd}, \tag{8}$$

where $D = \{(\mathbf{x}_{sat}, \mathbf{x}_{bkgd}) | g(\mathbf{x}_{sat}, \mathbf{x}_{bkgd}) < v\}$ such that the integral is taken over the space of orbital parameters where the MOID is less than the threshold v. Eq. (8) can be numerically approximated via Monte-Carlo integration by uniformly sampling points from the domains of the distributions of X_{sat} and X_{bkgd} and finding the points where the MOID is less than the threshold value. This is calculated as

$$P(\text{MOID} < v) = \frac{1}{N} \sum_{i=1}^{N} \left(p_{X_{sat}}(\mathbf{x}_{sat}^{(i)}) p_{X_{bkgd}}(\mathbf{x}_{bkgd}^{(i)}) (g(\mathbf{x}_{sat}^{(i)}, \mathbf{x}_{bkgd}^{(i)}) < v) V_{sat} V_{bkgd} \right), \tag{9}$$

where N is the number of samples used to integrate, $\mathbf{x}_{sat}^{(i)}$ and $\mathbf{x}_{bkgd}^{(i)}$ are orbital parameters sampled from the domains of the distributions of X_{sat} and X_{bkgd}, $(g(\mathbf{x}_{sat}^{(i)}, \mathbf{x}_{bkgd}^{(i)} < v)$ is 1 when the MOID is less than the threshold and 0 otherwise, and V_{sat} and V_{bkgd} are the volumes of orbital parameters over which the distributions are sampled. In the case of a single object, V_{sat} is the volume of a hyperellipsoid with radius 6σ in each direction, where σ is the variance of the relevant orbital parameter. Samples from the background population are taken from a range of each parameter, so V_{bkgd} is the volume of a hypercuboid with side lengths of the range of each parameter. The calculation of the MOID between two samples of orbital parameters uses a fast implementation to maintain the overall speed of the method (Wizniowski and Rickman, 2013).

To account for the number of objects in the population, the probability is scaled to give the collision likelihood:

$$l_{col} = N_{sat} \cdot N_{bkgd} \cdot P(\text{MOID} < v), \tag{10}$$

where N_{sat} is the number of objects in the mission of interest for which the risk is calculated and N_{bkgd} is the number of objects in the background population. This value gives a measure of the likelihood of collisions between two populations of objects.

3.3. Encountered severity

The encountered severity is the effect of a collision on the mission of interest. This effect can range from slight degradation in performance to complete loss of the mission and so it is important to distinguish between these types of collisions. The proposed encountered severity factor divides collisions into three levels of severity – low, medium, and high – depending on the mass of the impactor. Two different threshold masses are defined: m_l is the threshold between low- and medium-severity and m_u is the threshold between medium- and high-severity.

High-severity collisions are defined here as catastrophic collisions that result in total breakup of the satellite. The NASA Standard Breakup Model (SBM) defines a threshold of 40 J/g as the relative energy above which a collision is catastrophic (Johnson et al., 2001). The relative energy of a collision is

$$E = \frac{1}{2}\frac{m_{chaser}}{m_{target}}v_{rel}^2, \tag{11}$$

where m_{chaser} and m_{target} are the chaser and target masses and v_{rel} is the relative velocity between the two objects. m_{target} is assumed to be known for a satellite in the mission of interest. v_{rel} is taken as a worst-case value of twice the circular orbit velocity at the altitude of the satellite, which assumes a direct head-on collision between the objects. Therefore the mass threshold m_u is the chaser mass in Eq. (11) that results in a relative collision energy of 40 J/g.

Medium-severity collisions are where the satellite experiences some damage but not catastrophic breakup. The threshold between low- and medium-severity collisions is very mission specific as it depends on the level of shielding used in the mission and the level of acceptable damage. Estimates of damage to a spacecraft from small impactors often use the diameter of the impactor as the defining characteristic. For consistency with the upper mass threshold, this diameter is converted into the lower mass threshold m_l assuming a spherical impactor:

$$m_l = \rho_c \frac{4\pi}{3}\left(\frac{d_c}{2}\right)^3, \tag{12}$$

where ρ_c is the density of the impactor (chaser) and d_c is the critical diameter of impactor that defines the boundary between low- and medium-severity. One approach to defining this threshold is to use Ballistic Limit Equations (BLEs), which give the minimum diameter of object required to penetrate a shield for specific collision and shield parameters. In the simplest case of a metallic single wall, the ballistic limit of diameter of chaser in a head-on collision is defined in (Ryan and Christiansen, 2010) as

$$d_c = \left[\frac{t_s}{1.8}\cdot\frac{\mathrm{HB}^{0.25}(\rho_c/\rho_t)^b}{5.24(v_{rel}/C)^{2/3}}\right]^{\frac{18}{19}}, \tag{13}$$

where HB, ρ_t, and C are parameters of the satellite (or shield) material, t_s is the wall thickness, ρ_c is the chaser object density, and the exponent b is 0.5 when $\rho_c/\rho_t < 1.5$ and 1.5 otherwise. Default values for these parameters are based on aluminium satellite material: $\mathrm{HB} = 73, \rho_t = 2.713\ \mathrm{g/cm^3}$, $C = 5.069\ \mathrm{m/s}, t_s = 1.5\ \mathrm{cm}$, and for the chaser $\rho_c = 2.8\ \mathrm{g/cm^3}$.

Low-severity collisions mostly occur for sizes of objects that are not trackable. To account for untracked objects, the background distribution of mass includes the ESA MASTER 2016 population of Micro-Meteoroids and Orbital Debris (MMOD) (Braun et al., 2021). The total number of background objects in the relevant orbit regime with mass $m < m_l$ used to calculate the low severity factor of encountered severity is denoted N_{low}. Similarly, the medium-severity calculation uses the number of objects N_{medium} where $m_l \leqslant m < m_u$ and for high-severity the number of objects N_{high} where $m \geqslant m_u$. The encountered severity factor defined here acts as a scaling of the collision likelihood as expressed in Eq. (10). For the estimated number of objects in each mass threshold across the relevant orbital regime, the low-, medium-, and high-severity factors for encountered severity are

$$sf_{low} = \frac{N_{low}}{N_{bkgd}}, \tag{14}$$

$$sf_{medium} = \frac{N_{medium}}{N_{bkgd}}, \tag{15}$$

$$sf_{high} = \frac{N_{high}}{N_{bkgd}}, \tag{16}$$

where N_{bkgd} is the number of tracked RSOs in the relevant snapshot of the environment. The product of each severity term with the collision likelihood gives the estimated likelihood of each level of encountered risk.

3.4. Induced severity

The induced severity is a measure of the increased risk to active payloads in the environment as a result of a collision. This is difficult to estimate since the number and distribution of payloads in the environment changes over time. Therefore, the proposed induced severity factor also depends on predicted future launches. Instead of propagating fragments for every potential collision event, the induced severity calculation fits a simple model to estimate the collision likelihood with fragments based on simulated events. The procedure for modelling the induced severity is as follows:

1. Simulate a number of fragmentations with the NASA SBM,
2. Propagate each fragment cloud for 10 years,
3. Determine a worst-case payload population based on the current population and 10-year launch model,
4. Find the collision likelihood between this population and each propagated fragment cloud,
5. Fit a function of the collision and environment parameters to estimate the collision likelihood for each fragment cloud – equivalent to the induced severity.

The first step is to run simulations of collisions in LEO, MEO, and GEO over a range of orbital and collision parameters. The relevant collision parameters are target and chaser masses and the relative velocity. Each scenario acts as an input to the NASA SBM to simulate fragmentation events. Using outputs from these simulated collisions, the fragments larger than 1 cm are propagated for ten years and a distribution fit to the propagated fragments. This time horizon allows the fragment band to spread across

the orbital shell in RAAN, at which point its distribution does not vary as substantially. In cases where the number of fragments larger than 1 cm is less than 100, multiple fragmentations are simulated to generate at least 100 fragments for creating a representative distribution.

As described in Section 2, the total number of objects launched each year can be modelled using Eq. (1) or (2). This is divided into object classes of Payloads, Rocket Bodies, and Mission Related Objects. When calculating the induced severity, we only consider Payloads. As a worst-case assumption, all currently active payloads and newly launched payloads over ten years are assumed to remain active. Therefore the future payload population is taken as the current payload population plus launched payloads.

With the populations of payloads and propagated fragments defined, the next step is to calculate the collision likelihood between these two populations. This is done using the same approach as described in Section 3.2 by fitting a GMM to propagated fragments and the payload population and finding the intersection via Eq. (9). The output of this is the probability of fragments from each simulated event colliding with the worst-case future payload population. These values are used as training data for the model of induced severity.

The final step in defining the induced severity factor fits a simple model to the simulated collision likelihoods with fragments. The features of a collision used to estimate the severity factor are:

- Equivalent mass M,
- Density of payloads ρ,
- Normalised object decay rate r_{decay}.

The equivalent mass comes from the NASA SBM and is defined as

$$M = \begin{cases} m_{target} + m_{chaser} & \text{if } E > 40J/g, \\ m_{chaser} \cdot \frac{v_{rel}}{1000} & \text{otherwise.} \end{cases} \tag{17}$$

The density of payloads comes from a kernel density estimate of the future payload population as defined above. The value of ρ is the probability density of the kernel density estimate at the relevant altitude, as shown in Fig. 19 for LEO, which is used since fragmentations in more densely populated altitudes are likely to cause more collisions. The kernel density estimate is fit to altitudes of the future payload population. In GEO, ρ is the sum of probability densities over altitude and RAAN, since the location in RAAN is more significant for these orbits.

The final feature is the decay rate, which only applies to objects in LEO. Over the 10-year propagation duration, a number of the fragments in each simulated scenario decay. The fraction remaining at the end of the propagation depends on the altitude as shown in Fig. 20. This trend can be captured using the log-exponential model of Eq. (1) by replacing the year t with the altitude h in metres.

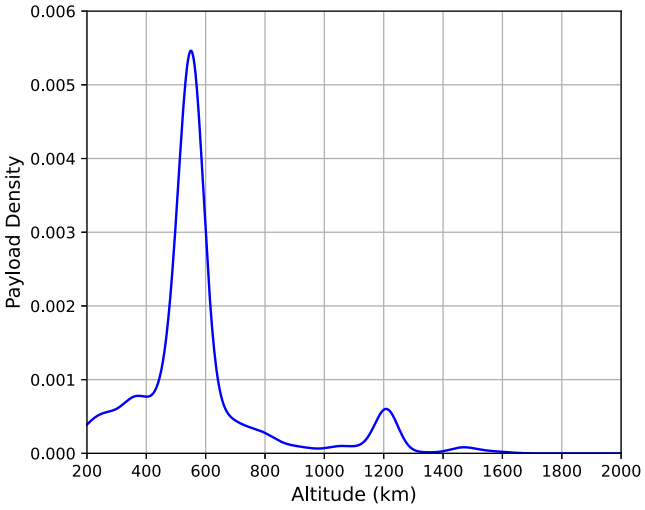

Fig. 19. Kernel density estimate over altitude of estimated future payload population in LEO.

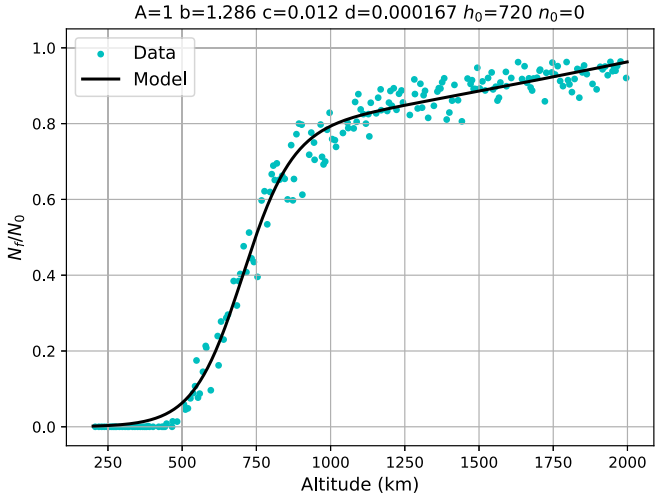

Fig. 20. Log-exponential model of decay rate of fragments in LEO.

The parameters shown are calculated using a least-squares fit.

The induced severity factor takes the following form:

$$sf_{induced} = a \cdot M^{0.75} \cdot \rho^{b} \cdot r_{decay}, \tag{18}$$

where a and b are coefficients calculated using a least-squares fit, M is the equivalent mass calculated from Eq. (17), ρ is the payload population density, and the decay factor $r_{decay} = 1$ except for LEO where it is calculated as described above.

4. Defining risk model parameters

The risk model defined above has certain parameters that affect its output. When calculating collision likelihood, this depends on the threshold MOID value and the induced

severity factor requires the generation of example fragmentations to fit the model. This section describes the process used to define these parameters.

4.1. Defining MOID thresholds

The threshold value v of the MOID has a substantial effect on the computed collision likelihood, since higher thresholds result in correspondingly higher probabilities. Measures of risk based on miss distance are common in conjunction analysis and there are other works relating these measures to probability of collision (Horwood et al., 2014). For a given conjunction event, the distance threshold d at which the maximum collision probability is P_{max} can be defined as

$$d = \sqrt{\frac{AR \cdot r^2}{\alpha}}, \tag{19}$$

where AR is the ratio of major-to-minor projected covariance ellipses (Alfano, 2013), r is the combined object radius, and α is defined in terms of the probability P_{max} as:

$$\alpha = \beta - \frac{40}{49\beta} + \frac{4}{7}, \tag{20}$$

$$\beta = \left(\frac{12eP_{max}}{7} + \sqrt{\frac{144(eP_{max})^2}{49} - \frac{6528eP_{max}}{2401} + \frac{2816}{2401}} - \frac{272}{343} \right)^{\frac{1}{3}}. \tag{21}$$

Typical values for the relevant parameters are $AR = 3$ and $r = 10m$ (Horwood et al., 2014; Alfano, 2013). Then the maximum probability of collision should be specified based on the desired threshold probability. Common thresholds for "high-risk" conjunctions range from 10^{-6} to 10^{-4} (Uriot et al., 2022). The analyses presented here use threshold values of 10.51 km, 3.32 km, and 1.05 km corresponding to maximum probabilities of $10^{-6}, 10^{-5}$, and 10^{-4}, respectively.

4.2. Tracking accuracy

In addition to the threshold MOID value, the assumed variance of the orbital parameters of the mission affects the calculation of collision likelihood. The uncertainty in the orbital elements depends on the assumed level of tracking accuracy of the mission. Table 1 lists the covariances associated with different levels of tracking accuracy when

Table 1
Variance values for orbital elements with different levels of tracking accuracy.

Tracking Accuracy	SMA (km)	Ecc.	Inc. (°)	Raan (°)	aPer (°)
Low	20	10^{-4}	10^{-3}	10^{-3}	10^{-3}
Medium	2	10^{-5}	10^{-4}	10^{-4}	10^{-4}
High	0.05	10^{-6}	10^{-5}	10^{-5}	10^{-5}

Table 2
Distribution of samples for generating example fragmentations.

	LEO			GEO		
	Sample	Min.	Max.	Sample	Min.	Max.
SMA (km)	Sobol	6571	8371	Sobol	42130	42200
Ecc.	0	–	–	0	–	–
Inc. (°)	Sobol	20	110	Sobol	0	15
RAAN (°)	Uniform	0	360	Sobol	0	360
True ano. (°)	Uniform	0	360	Sobol	0	360
V rel. (km/s)	Gamma	$16 - \Gamma(4, 1.67)$		Sobol	0	0.8
M target (kg)	Sobol (log)	10^1	10^4	Sobol (log)	10^2	10^4
M chaser (kg)	Sobol (log)	10^{-2}	$0.1M_t$	Sobol (log)	10^2	10^4
	MEO ex. NSO			NSO		
	Sample	Min.	Max.	Sample	Min.	Max.
SMA (km)	Sobol	8500	20000	Sobol	25000	30000
Ecc.	Sobol	0	0.05	Sobol	0	0.01
Inc. (deg)	Sobol	0	130	Sobol	50	70
RAAN (deg)	Uniform	0	360	Uniform	0	360
True ano. (deg)	Uniform	0	360	Uniform	0	360
V rel. (km/s)	Sobol	4	$2v_{orbit}$	Sobol	4	$2v_{orbit}$
M target (kg)	Sobol (log)	$10^{2.5}$	$10^{3.5}$	Sobol (log)	$10^{2.5}$	$10^{3.5}$
M chaser (kg)	Sobol (log)	10^{-2}	$10^{1.5}$	Sobol (log)	10^{-2}	$10^{1.5}$

modelling the distribution of a mission. These values are based on those presented for equinoctial elements in (Horwood et al., 2014), which are assumed to be similar for the Keplerian elements used here. (see Table 2).

4.3. Simulated fragmentations

In each regime, fragmentations were simulated for a range of orbital parameters and masses covering typical values in the respective regime. Most parameters used a Sobol sampling strategy to ensure good coverage across these parameters. In LEO, a gamma distribution was found to give a reasonable approximation of the expected distribution of relative velocities. Example fragmentation scenarios in MEO were also divided into regimes including and excluding Navigation Satellite Orbit (NSOs) to give particular focus to this more densely populated region. All fragment propagations used the ESA DELTA model with all force models enabled (Virgili, 2016).

4.4. Induced severity factor fit

When calculating the collision likelihood between fragments and the future payload population, all models use a MOID threshold of $v = 3.32$ km. Fig. 21 shows the LEO induced severity factor fit with confidence bounds. Points used in fitting the model are shown with the x-coordinate as the model output and the y-coordinate as the "true" induced severity factor from simulation. For a perfect model, all points would lie on the line $y = x$. As indicated in the plot, the true values are spread around the model fit which is captured by the 95% confidence interval. Although this interval on the log scale is large relative to the magnitude of severity, the combination of input parameters successfully captures the overall trend in the probability of collision of the fragments.

Using the same process as LEO without the decay rate, the severity factors for MEO and GEO were derived as shown in Fig. 22 and Fig. 23. For GEO, the model was improved by including a density term for RAAN as well as altitude. As with the altitude density, the RAAN density comes from the kernel density estimate over RAAN of payloads in GEO. In the MEO and GEO regimes the accuracy of the severity factor model is lower than in LEO. However, they still show an overall trend of increasing estimated severity factor with increased probability of collision. With the corresponding confidence limits, these models can give a coarse estimate of the induced risk of a mission.

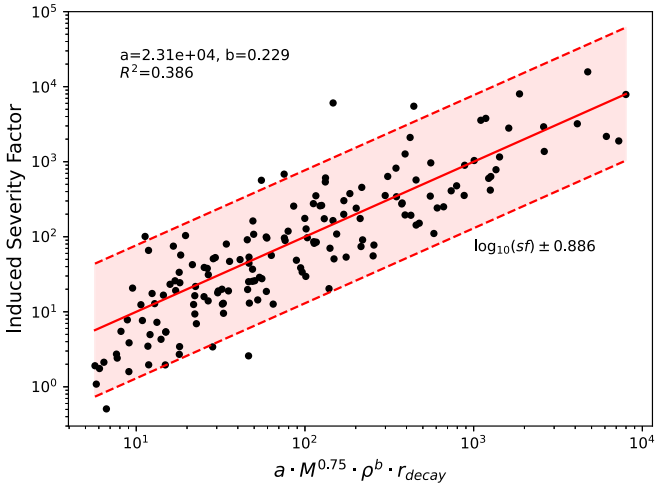

Fig. 21. Induced severity factor fit and confidence bounds in LEO.

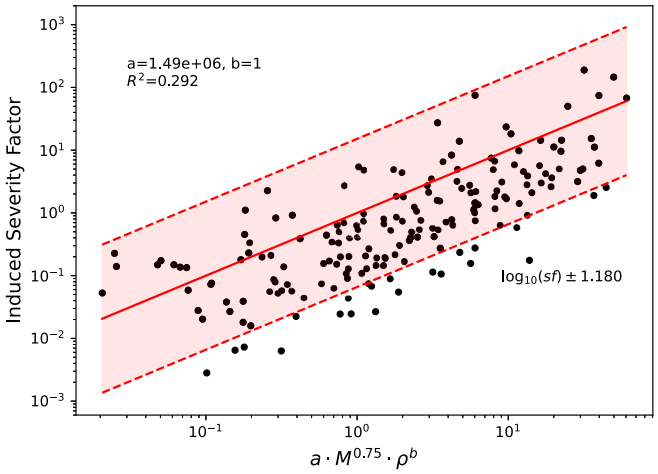

Fig. 22. Induced severity factor fit and confidence bounds in MEO.

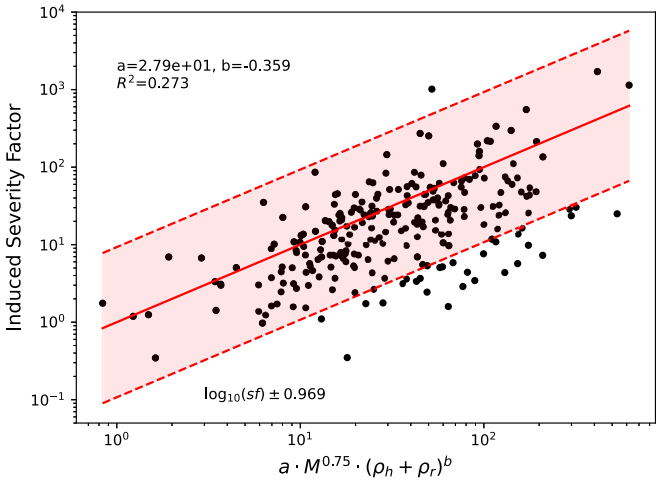

Fig. 23. Induced severity factor fit and confidence bounds in GEO.

5. Future space environment simulations

The parametric model of launches introduced in Section 2 gives a highly flexible method for simulating future launch traffic. This is demonstrated here by showing some example launch scenarios using this model. Each of these launch scenarios were added to a propagation of the space environment to show how different assumptions on future launches affect the evolution of the environment. Simula-

tions were run using ESA's DELTA software with all force models in the propagator and fragmentations resulting from collisions and explosions. The dates simulated were from 2023 until 2074 with snapshots of the population taken for each year of the simulation.

This study uses three different launch scenarios that are herein referred to as no launches, realistic, and unrealistic. Table 3 lists the launch model parameters for the realistic and unrealistic scenarios. These parameters and the associated outputs of DELTA simulations are the results of previous work investigating different environment evolution scenarios using the tool DORAS (McNally et al., 2024). The models for the total number of objects launched for LEO and GEO use Eq. 1 and for MEO Eq. 2. In LEO, this trend excludes constellation payloads, which are added separately based on planned future constellations. The following sections describe the effect of the different launch models on the environment simulations.

5.1. LEO

As discussed above, constellations can be included in the overall launch model or defined separately. Table 4 shows 6 of the largest current and planned constellations, including missions that already have a substantial number of operational payloads. The deploy start gives the approximate date when the satellites begin launching, assumed to be the first of January of that year, and the mission start is when all satellites in the constellation are assumed to be launched and operational. Based on the number of spacecraft in a constellation and lifetime of each spacecraft, it is possible to estimate the necessary number of objects launched per year to maintain the constellation from the mission start date. Combined with the modelled launches excluding constellations, this gives an estimate of the total number of objects launched in future.

Fig. 24 shows the assumed total number of payloads launched per year from the constellations in Table 4, excluding the ramp up time from deployment start. This only considers the average number of launches each year to replace spacecraft at the end of their lifetime. After 2027, the number of constellation payloads launched remains constant at 2243 per year, assuming the constellations remain operational and continue to replace satellites.

Fig. 25 shows the launch models for all object types to LEO excluding constellations. These result in trends in the total number of objects as shown in Fig. 26, which includes the constellation payloads. In these simulations, the number of objects remains near constant with no launches and increases steadily for the scenarios with launches.

Table 3
Launch model parameters for different scenarios in each orbital regime.

Regime	Scenario	A	b	c	d	t_0	n_0
LEO	Realistic	1100	0.8	0.2	0.002	2025	100
	Unrealistic	2000	1.3	0.4	0.03	2024	150
MEO	Realistic	0.8	-	-	-	-	5
	Unrealistic	1.8	-	-	-	-	10
GEO	Realistic	−12	1	0.3	0.0001	2030	23
	Unrealistic	50	1.8	0.9	0.008	2025	25

5.2. MEO

Fig. 27 shows the launch models for all object types to MEO, which both use the simpler linear model. The trends in the number of objects in this region are shown in Fig. 28. Similarly to LEO, both launch scenarios show a substantial increase in number of objects compared to no launches, however this increase occurs less gradually and mostly towards the end of the simulation period.

5.3. GEO

Fig. 29 shows the launch models for all object types to GEO. Unlike the other regimes, the realistic scenario assumes a slight decrease in the number of objects launched to this regime in the future. As shown in Fig. 30, the number of objects in GEO varies less substantially depending on the launch model than in the other regimes.

6. Risk calculation for example missions

This section presents example applications of the risk model in the environment scenarios described above. The example missions used here are described in Table 5. This shows the orbital parameters, mass, and number of satel-

Table 4
Parameters of some planned constellations.

Name	Number of Spacecraft	Deploy Start	Mission Start	Lifetime (years)	Mass (kg)	SMA (km)	Ecc.	Inc. (°)
OneWeb	648	2020	2023	10	147	7578	1e-4	87.9
Starlink	8064	2020	2023	5	386	6938	1e-4	53
Spire Global	110	2020	2023	2	5	6868	1e-4	51.6
Amazon Kuiper	3264	2024	2025	7	650	6988	1e-4	51.9
Telesat	300	2026	2027	10	700	7626	1e-4	50.88
Boeing	147	2026	2027	10	3000	7463	1e-4	50

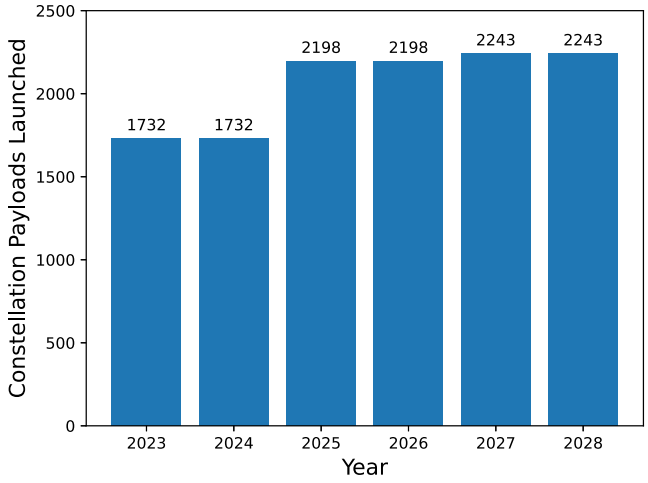

Fig. 24. Forecast number of constellation payload launches.

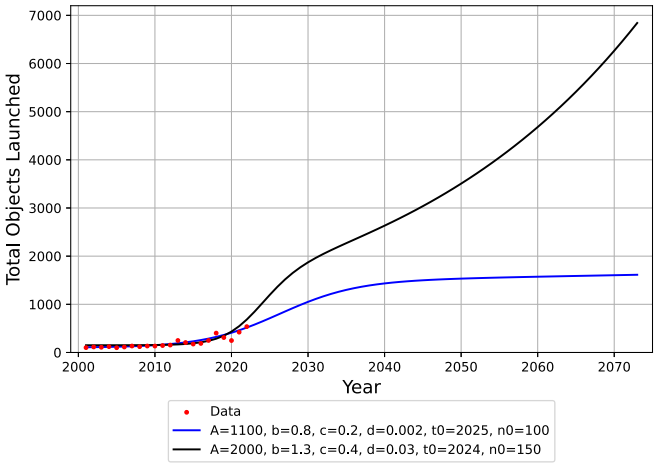

Fig. 25. Launch scenarios in LEO.

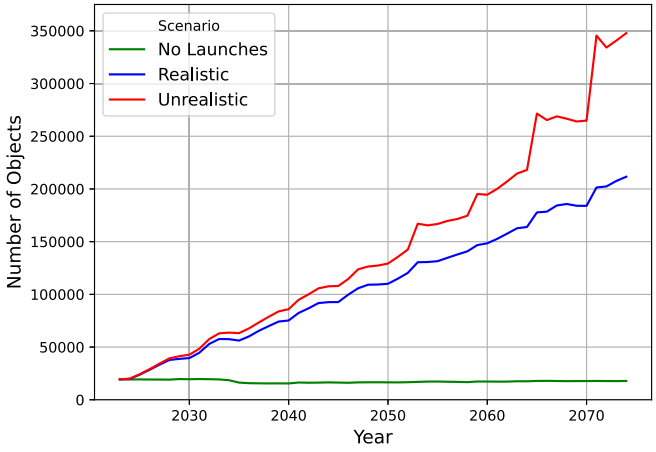

Fig. 26. Total number of objects in each scenario over the simulation duration in LEO.

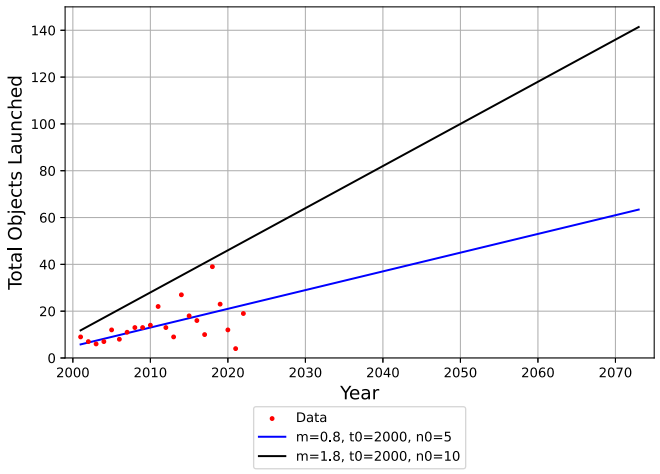

Fig. 27. Launch scenarios in MEO.

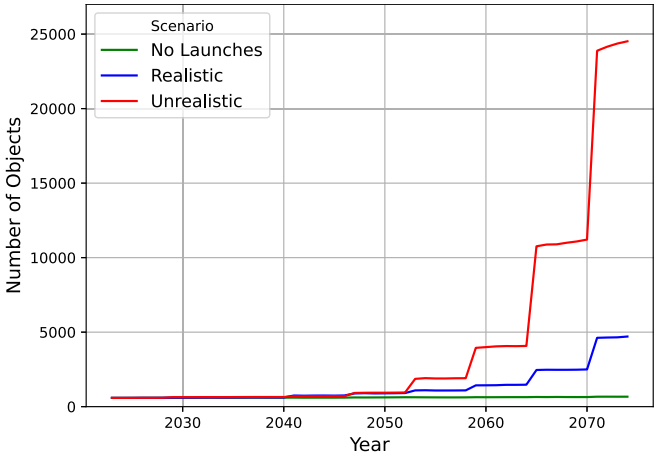

Fig. 28. Total number of objects in each scenario over the simulation duration in MEO.

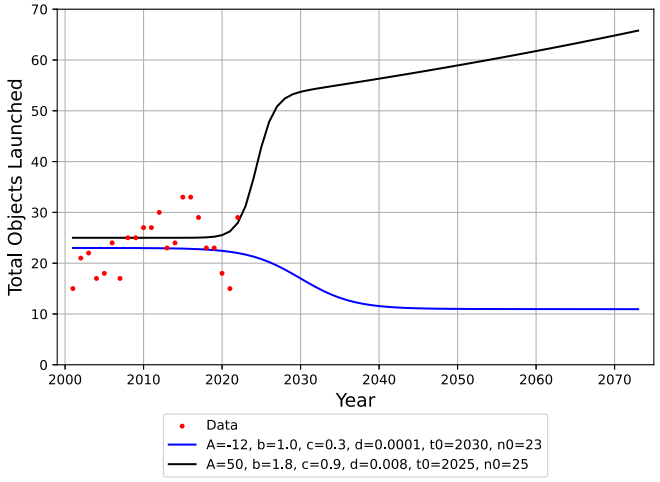

Fig. 29. Launch scenarios in GEO.

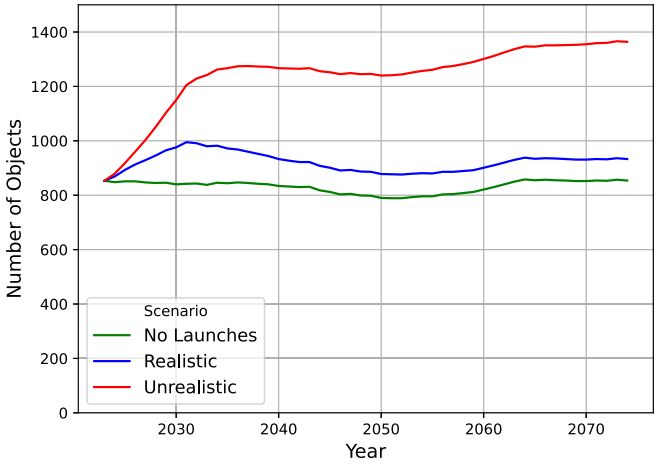

Fig. 30. Total number of objects in each scenario over the simulation duration in GEO.

lites for each example scenario. These examples cover orbits in LEO, MEO, and GEO and include an example constellation of 1000 satellites in LEO. In addition, we show a comparison of the proposed metric with another risk metric applied to orbits across LEO.

6.1. Varying model parameters

Section 4 defined three different MOID thresholds and three different values of variance in orbital elements for the risk calculation. These reflect different assumptions on the level of allowable collision probability and the level of tracking accuracy of the mission. Using Orbit 1 as a test case, we initially calculated the collision likelihood l_{col} for each combination of parameters to observe their effect on the likelihood. This used population snapshots from 2023 and 2074 of the realistic scenario. The results of this analysis are shown in Fig. 31.

The clear trend shown in Fig. 31 is an increase in collision likelihood, l_{col} with increasing MOID threshold and a decrease in l_{col} with increasing tracking accuracy, as is expected. For each level of tracking accuracy, the difference in l_{col} between the lowest and highest MOID threshold is around one order of magnitude. In this case the tracking accuracy has a more substantial effect on l_{col}, where the difference between the low and high tracking accuracies is around two orders of magnitude. These effects of varying the parameters are consistent in both snapshots, with generally higher collision likelihoods in 2074 mainly due to the increased numbers of objects. This suggests that changing

Table 5
Orbital parameters and masses of example missions.

Orbit	Regime	SMA (km)	Ecc.	Inc. (°)	Raan (°)	aPer (°)	mass (kg)	N_{sat}
1	LEO	6780	0.0005	52	–	–	10	1
2	LEO	6650	0.002	41	–	–	2	1
3	LEO	7250	0.0001	80	–	–	500	1
4	LEO	7800	0.05	70	–	–	500	1
5	MEO	15500	0.2	42	–	–	1000	1
6	NSO	26000	0.001	65	–	–	1000	1
7	GEO	42165	0.0005	0.5	270	270	1000	1
8	LEO	6971	0.0001	50	–	–	200	1000

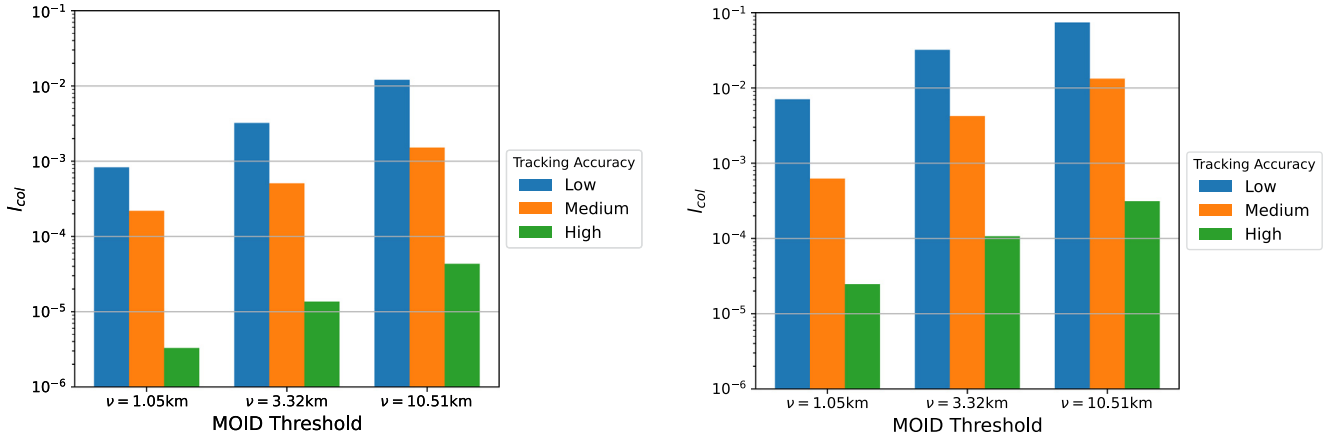

(a) 2023 (b) 2074

Fig. 31. Probability of collision with background population for different levels of mission tracking accuracy and MOID threshold.

the parameters of the model will change the scaling of the likelihood while maintaining a similar trend over different snapshots. The following results all use a MOID threshold of $v = 3.32$ km and assume a medium level of tracking accuracy.

6.2. Collision likelihood

Figs. 32–39 show the variation in collision likelihood l_{col} over time for each of the environment scenarios. With the exception of orbit 7 in GEO, these are all shown on log-scales to better highlight the trends. The orbits in LEO mostly follow a similar trend where the likelihood remains fairly consistent for the no launches scenario and increases substantially in the scenarios with launches. This trend is less noticeable for Orbit 3, where the values of l_{col} are similar across the scenarios for most of the simulated period. This would indicate that, for this orbit, the distribution of objects has a greater effect on the likelihood than the number of objects.

In MEO, the trend in collision likelihood for orbit 5 is similar to those of LEO, but at a lower order of magnitude due to the lower number of objects. Most trends show fluctuations in likelihood over time due to the stochastic nature of the model and this is particularly noticeable for orbit 6. In the NSO region, the estimated collision likelihood is sensitive to slight changes in the distribution of objects in this region which is the reason this trend varies so much

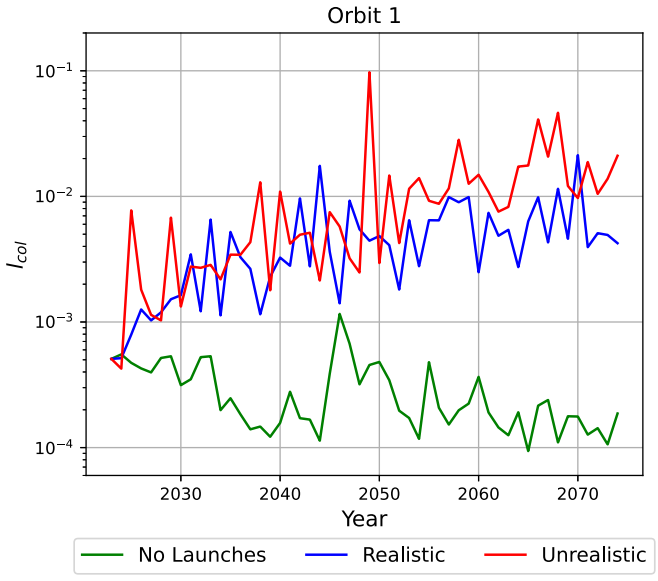

Fig. 32. Collision likelihood trend for orbit 1.

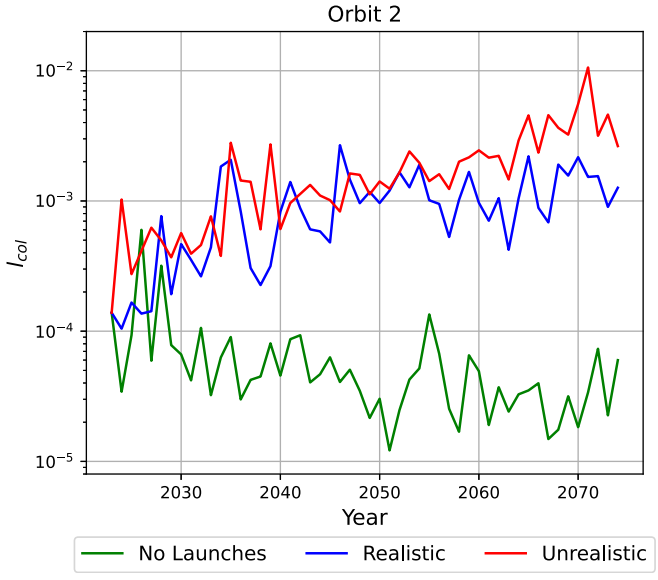

Fig. 33. Collision likelihood trend for orbit 2.

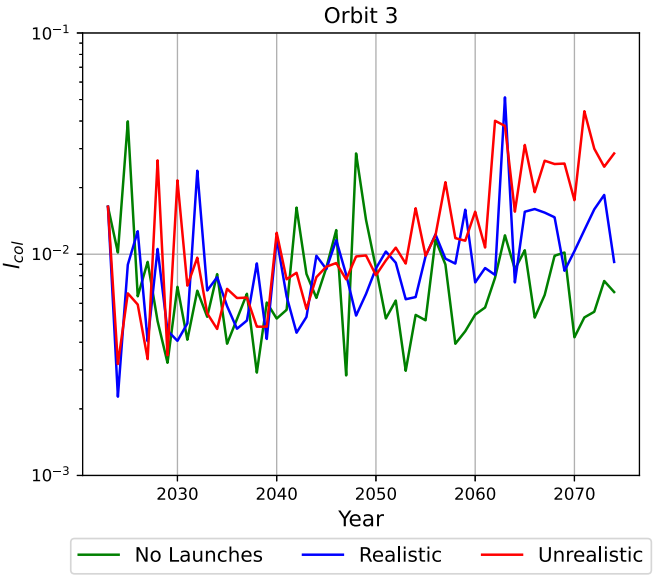

Fig. 34. Collision likelihood trend for orbit 3.

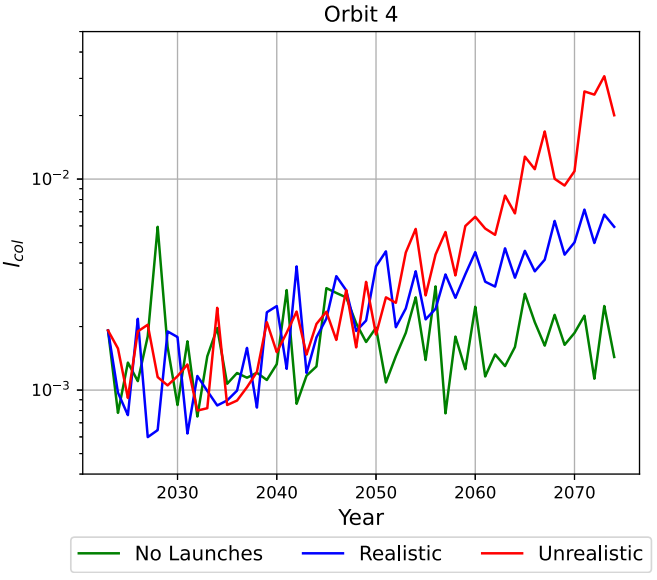

Fig. 35. Collision likelihood trend for orbit 4.

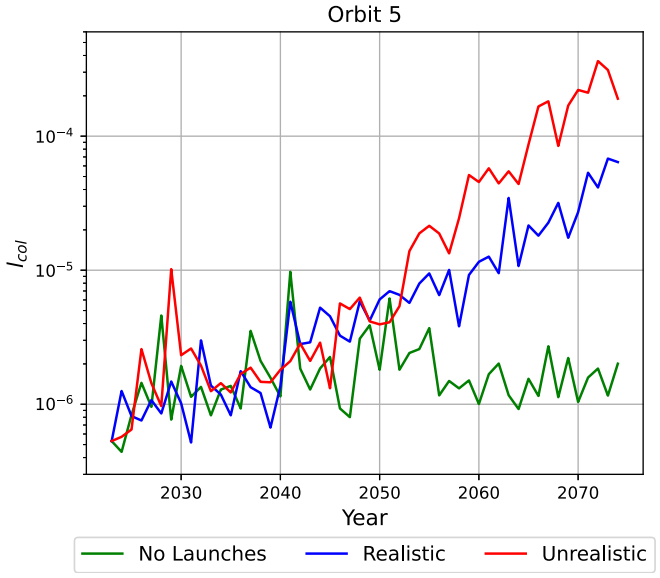

Fig. 36. Collision likelihood trend for orbit 5.

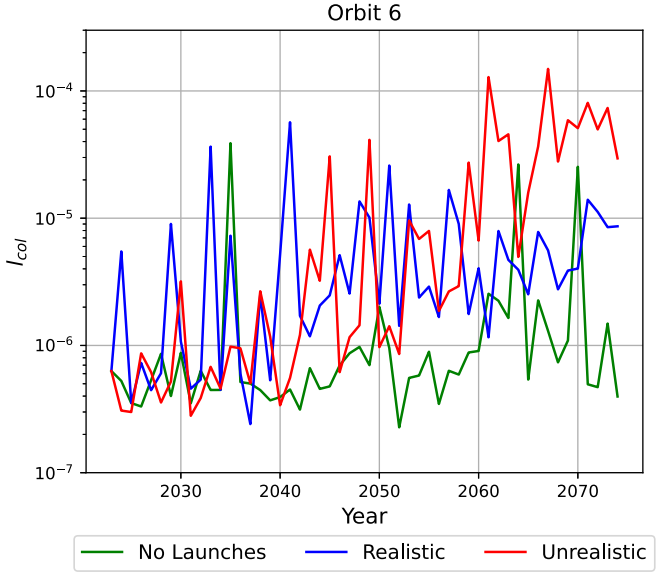

Fig. 37. Collision likelihood trend for orbit 6.

between snapshots. Similarly, orbit 7 sees several sudden increases in l_{col} at different snapshots across the scenarios. However, in this case the values of l_{col} all stay within the same order of magnitude and this orbit generally shows the least difference between the launch scenarios.

Orbit 8 comprises the constellation of 1000 satellites and so this has high values of l_{col} in the range of 1–100. Although the value of $p(\text{MOID} < v)$ in the calculation of collision likelihood is a probability that must lie between 0 and 1, the scaling by the number of objects can result in much larger values of l_{col}. Other than the order of magnitude, the trend in l_{col} is similar to the other orbits in LEO with a fluctuating value that does not substantially change in the no launches scenario and a significant increase with launches.

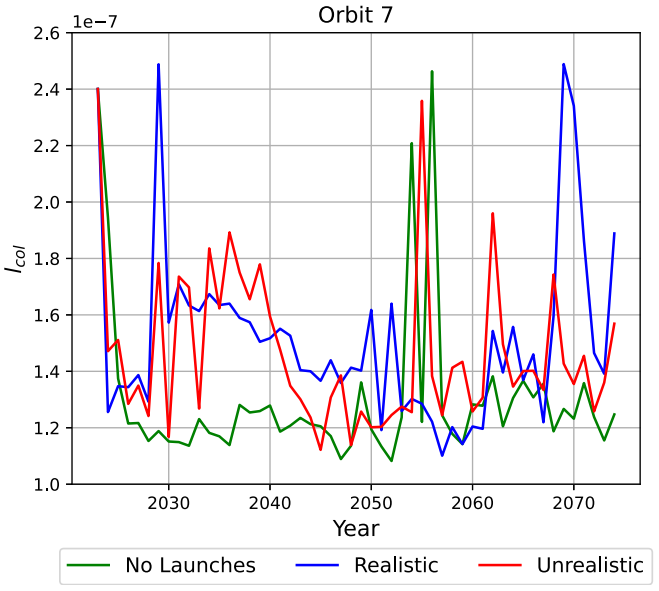

Fig. 38. Collision likelihood trend for orbit 7.

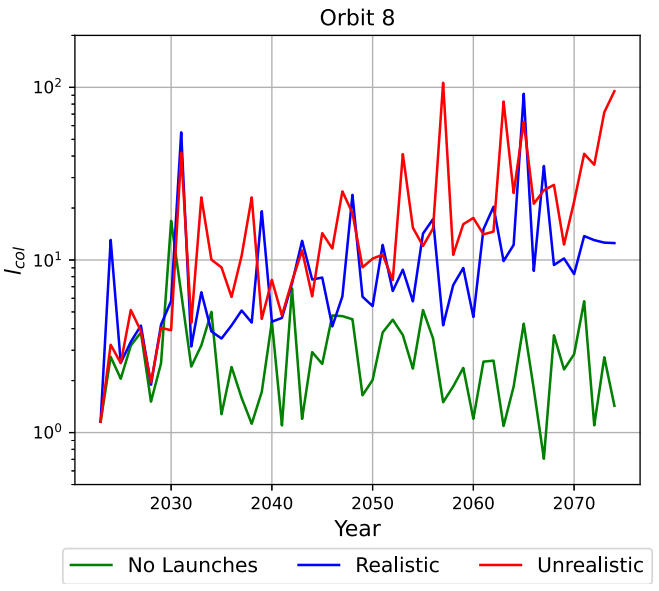

Fig. 39. Collision likelihood trend for orbit 8.

6.3. Encountered risk

Each example mission has three different levels of encountered risk that vary over time. These are shown in Figs. 40–47, where the line style indicates the level of encountered severity. The estimated number of objects includes the untracked objects, which are taken from the MASTER 2016 population (Braun et al., 2021). Using future extrapolations of the untracked debris environment would give more realistic estimates of the encountered severity, but this has not been done for this study.

Since the encountered risk is a scaled value of the collision likelihood, this trend is often similar to that of the collision likelihood. The most notable difference is in orbits 3

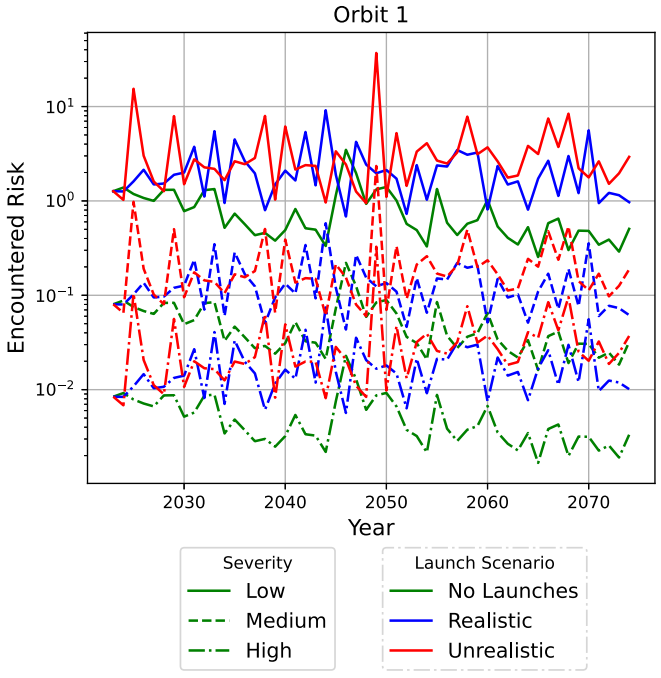

Fig. 40. Encountered risk trend for orbit 1.

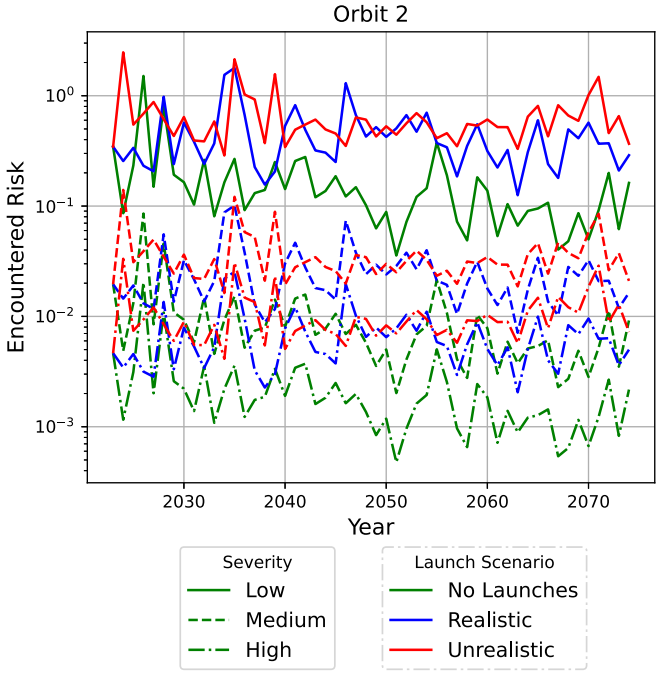

Fig. 41. Encountered risk trend for orbit 2.

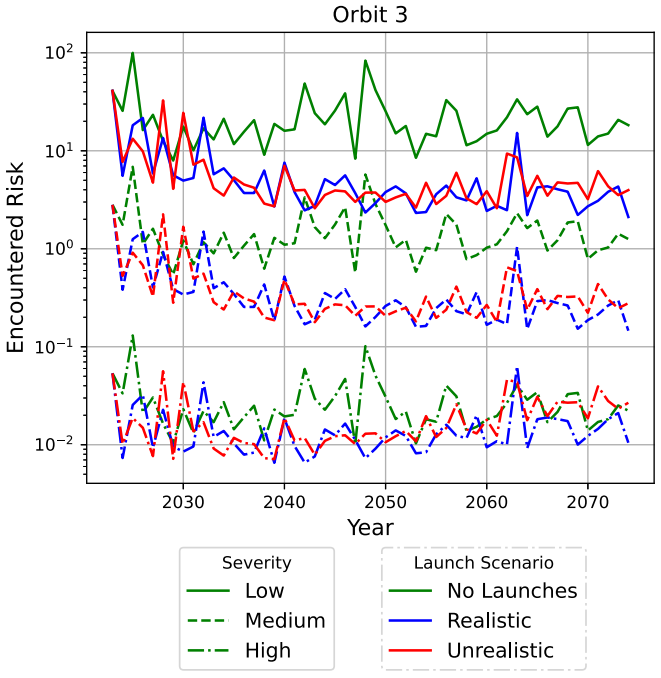

Fig. 42. Encountered risk trend for orbit 3.

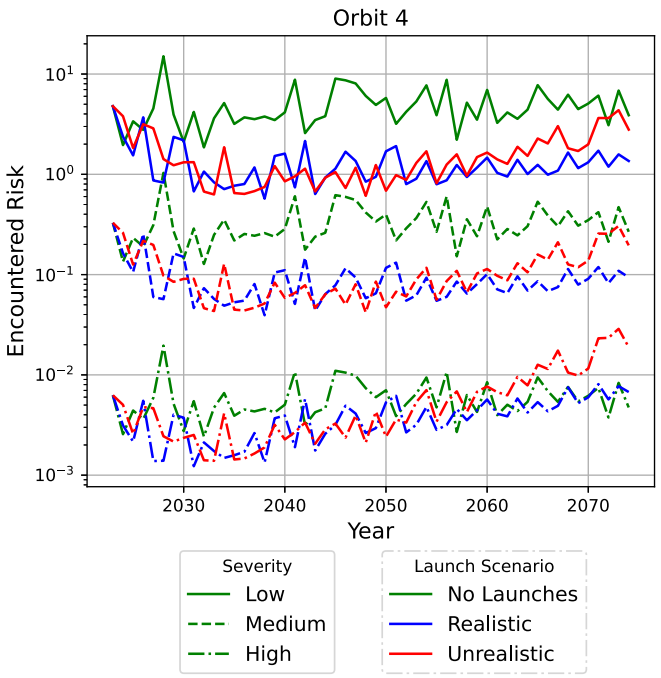

Fig. 43. Encountered risk trend for orbit 4.

and 4, where the low and medium encountered severity is generally higher in the scenario without launches than the scenarios with launches. Since the population of untracked objects remains constant in this calculation of encountered severity, the scaling is similar for all scenarios at the lower values of encountered severity. Therefore, it is the difference in distributions of objects that makes the difference in values of encountered risk. In orbits 3 and 4 in higher LEO, the relative density of objects tends to reduce and so the encountered risk also decreases.

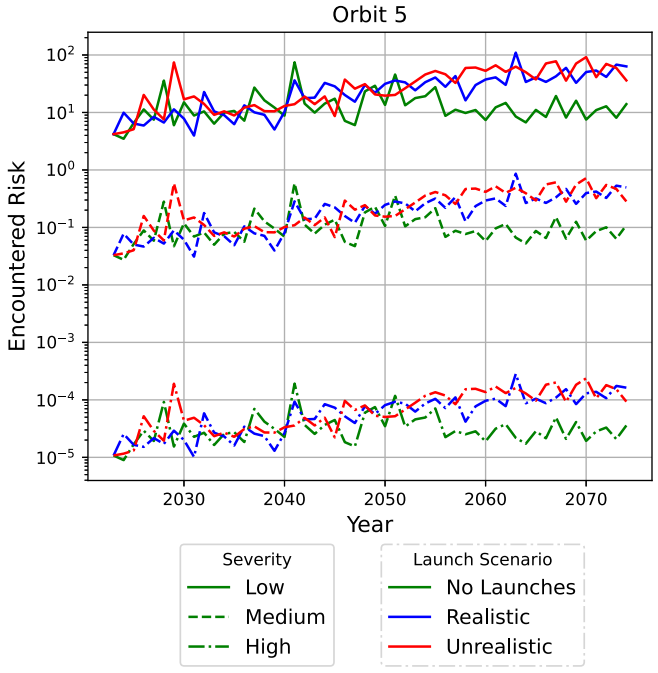

Fig. 44. Encountered risk trend for orbit 5.

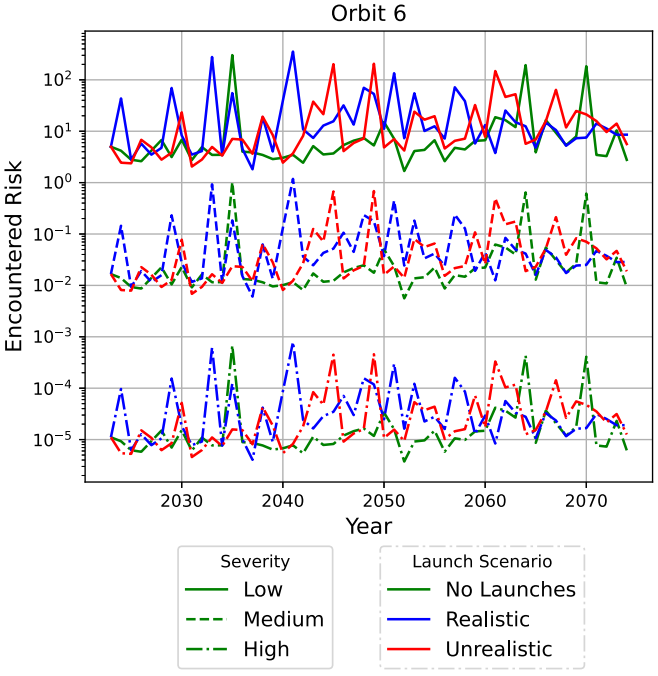

Fig. 45. Encountered risk trend for orbit 6.

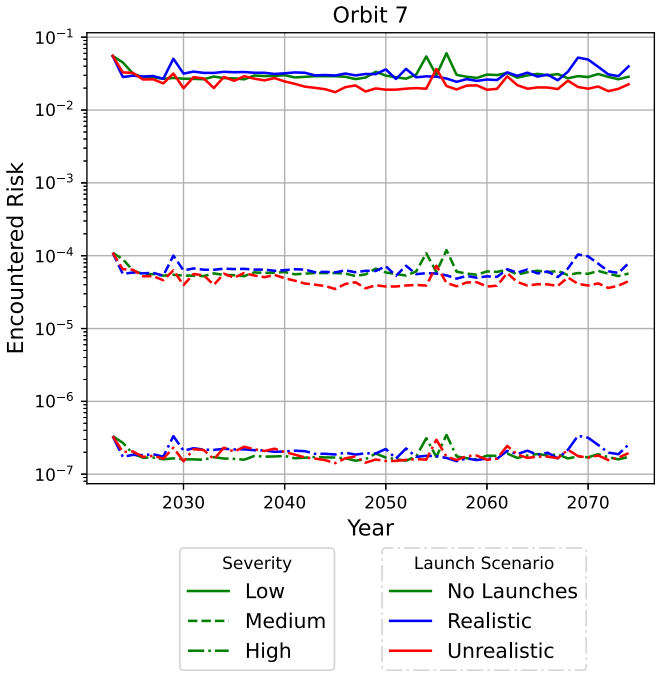

Fig. 46. Encountered risk trend for orbit 7.

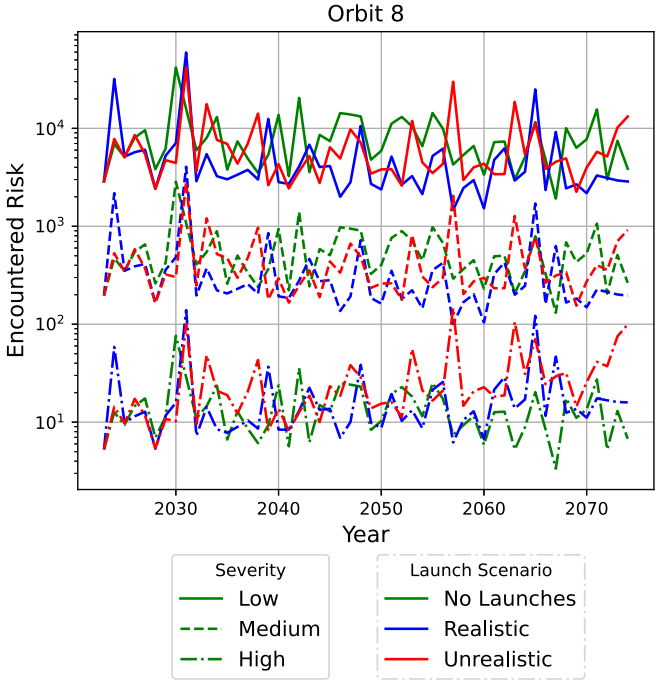

Fig. 47. Encountered risk trend for orbit 8.

6.4. Induced risk

When calculating the induced risk, the chaser mass is assumed to be the median mass of all tracked objects in the relevant regime in the 2023 population. This gives chaser masses of $m_c = 28.85$ kg in LEO, $m_c = 1050$ kg in MEO, and $m_c = 2964$ kg in GEO. LEO has a much lower median mass of tracked objects than MEO and GEO due to the large number of tracked small fragments in this regime. The values of equivalent mass M and decay rate r_{decay} remain constant for each orbit over the simulated time and only the projected future density of payloads varies. Figs. 48–55 show the variation in induced risk over time for each of the environment scenarios. In most cases,

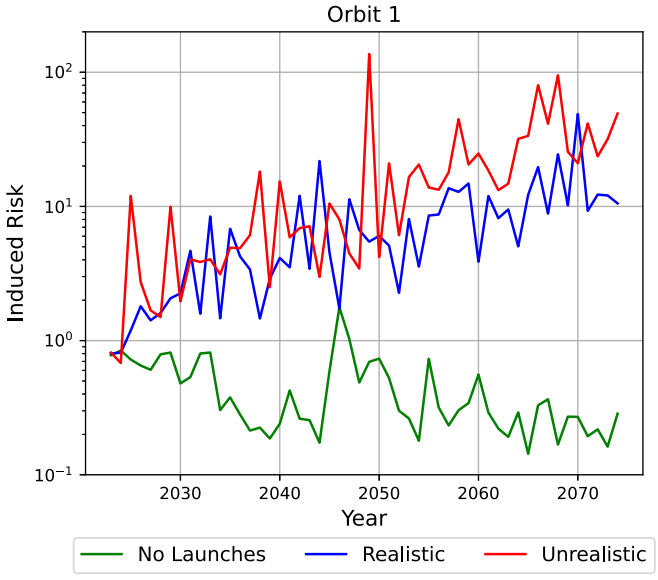

Fig. 48. Induced risk trend for orbit 1.

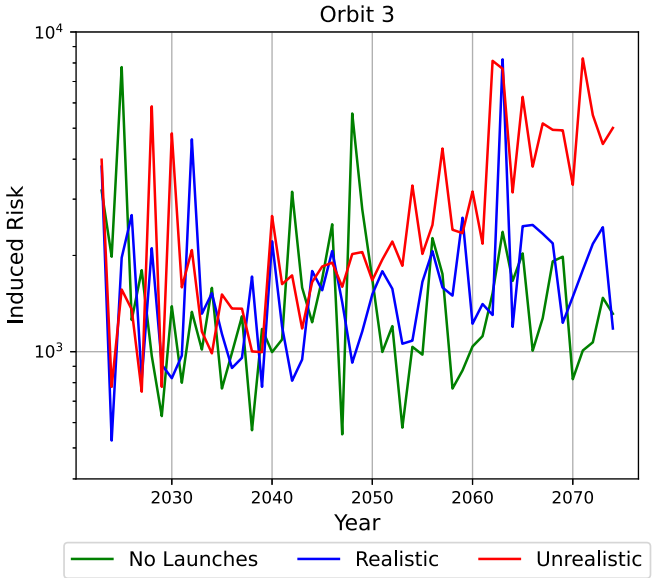

Fig. 50. Induced risk trend for orbit 3.

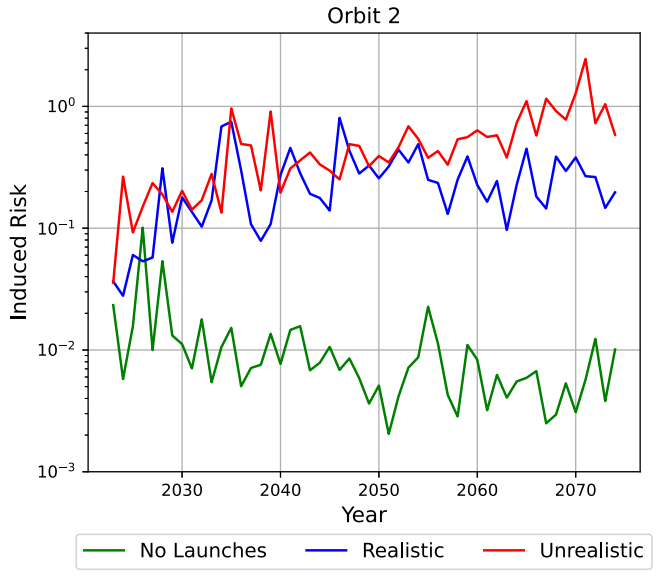

Fig. 49. Induced risk trend for orbit 2.

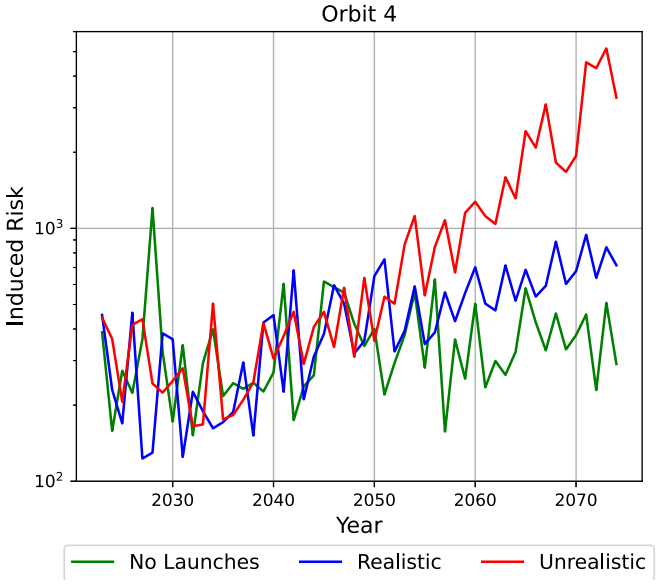

Fig. 51. Induced risk trend for orbit 4.

these trends are similar to that of the collision likelihood, but at a much higher order of magnitude due to the scaling by number of fragments. Orbits 1 and 2 in lower LEO have generally lower collision likelihoods than orbits 3 and 4 in higher LEO. In the induced risk trends, this difference is magnified by the r_{decay} term, which is much smaller for the lower orbits.

6.5. Comparison with ECOB

Here we compare the output of our model with the Environmental Consequences of Orbital Breakups (ECOB) index (Letizia et al., 2017) as implemented in the ESA debris index frontend[2]. This index is also risk-based and calculates the product of a likelihood term and a severity term. To compare the outputs of each model, we calculate the risk for orbits over a grid of altitudes between 400 km and 2000 km and inclinations between 0° and 140°. The purpose of this comparison is to show how the different modelling assumptions used in each metric affect the estimated distribution of risk over the environment.

When calculating collision liklehood, all orbits were considered near-circular with eccentricity 10^{-4}. The background population used to calculate event likelihood in this

[2] https://index.sdo.esoc.esa.int/

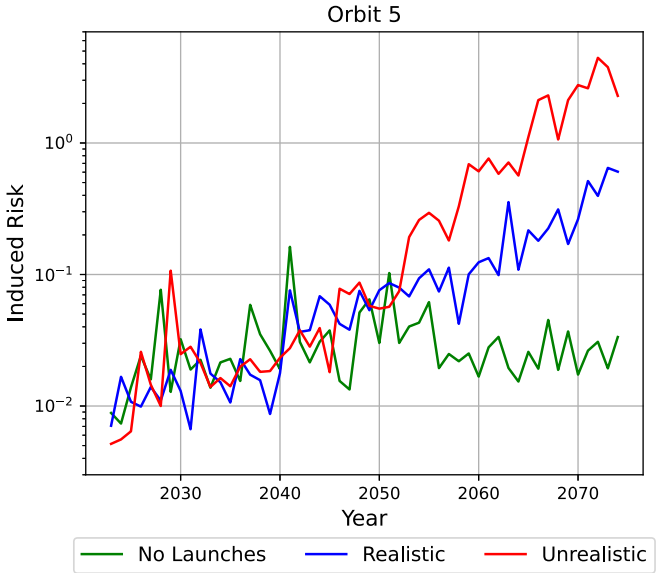

Fig. 52. Induced risk trend for orbit 5.

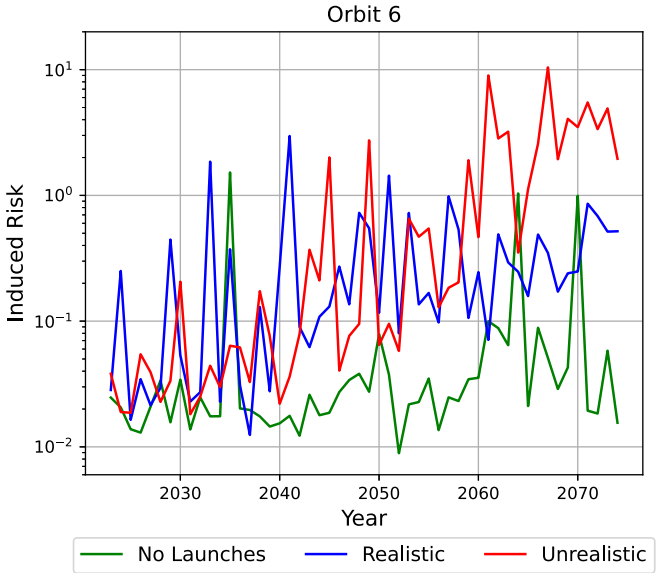

Fig. 53. Induced risk trend for orbit 6.

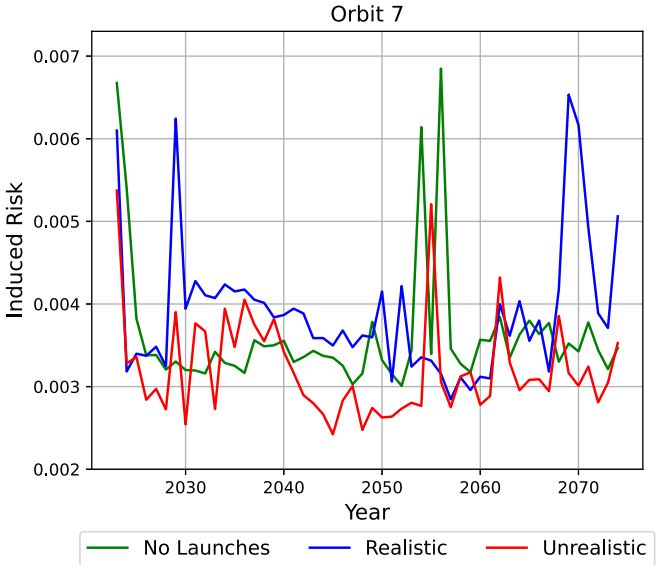

Fig. 54. Induced risk trend for orbit 7.

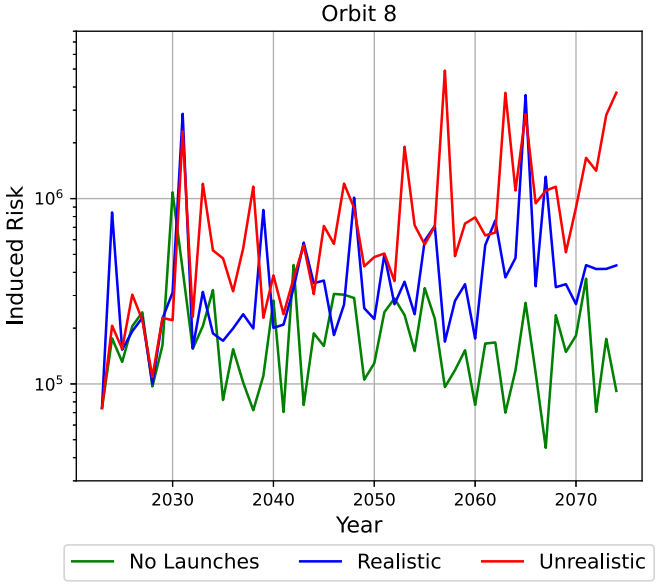

Fig. 55. Induced risk trend for orbit 8.

implementation of ECOB is the 2016 MASTER reference population. To give a reasonable comparison, we used tracked objects from DISCOSWeb at the reference epoch of 1 November 2016 as the background population when calculating collision likelihood. The calculation of severity used the current population of payloads from DISCOSWeb with no further launched objects. ECOB requires additional inputs related to the spacecraft and mission. We assume a spacecraft with a mass of 500 kg and area 5 m^2 and no collision avoidance capabilities. The Post Mission Disposal (PMD) success rate was set as 100% with a target end-of-life altitude of 0 km, i.e. controlled reentry.

Table 6 shows summary statistics of the values of each risk metric. ECOB gives lower values of risk compared to our metric, which directly scales with the number of objects resulting in larger values. Figs. 56 and 57 show the normalised values of ECOB and our risk metric, respectively, over the range of altitudes and inclinations considered. Both metrics show a band of higher risk at an altitude of 800 km. Since the induced severity factor does not account

Table 6
Statistics of both risk metrics applied to values of altitude and inclination across LEO.

Metric	Min.	Mean	Max.
ECOB	4.94×10^{-8}	3.36×10^{-6}	3.06×10^{-5}
$l_{col}sf_{induced}$	1.06×10^{-4}	8.43×10^{1}	1.02×10^{3}

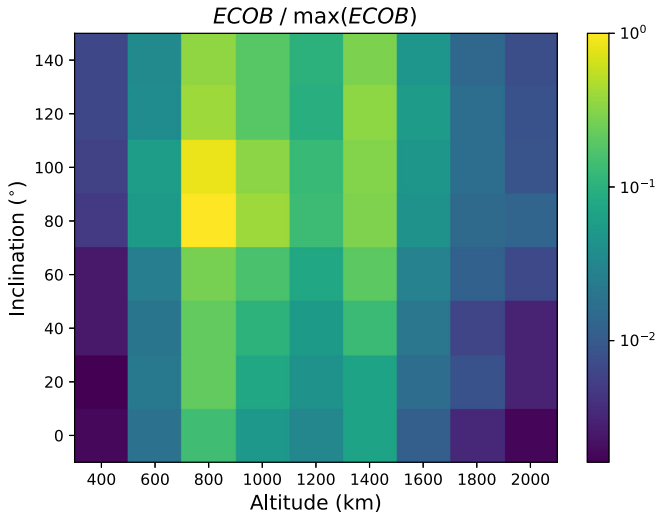

Fig. 56. Normalised ECOB over altitude and inclination.

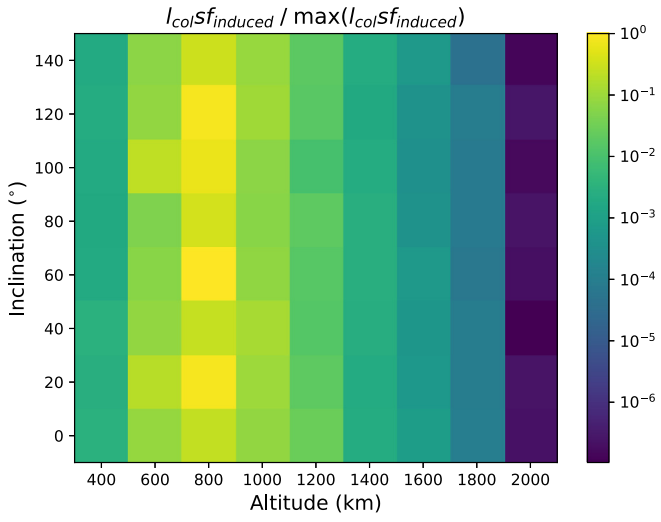

Fig. 57. Normalised risk metric over altitude and inclination.

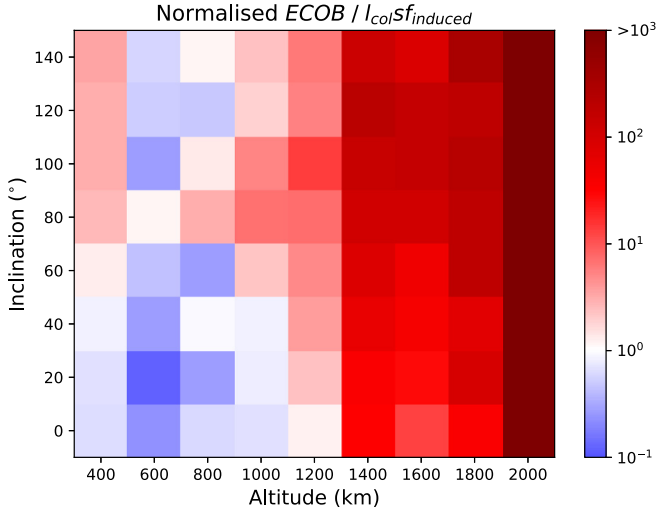

Fig. 58. Comparison of magnitudes of both normalised metrics.

for inclination, the value of our risk metric does not vary substantially with inclination. In addition, higher orbits have lower densities of objects and hence lower risk due to both l_{col} and $sf_{induced}$ being lower. This is the most noticeable difference in the plots, where for altitudes greater than 1200 km our risk metric tends to decrease sharply, whereas ECOB sees an additional region of higher risk at 1400 km.

Fig. 58 shows the difference in orders of magnitude of both normalised metrics. This clearly shows that the normalised values are generally similar at altitudes below 1200 km, whereas above this altitude ECOB gives much larger normalised values. Since the reference population used for our metric only consists of tracked objects, this will affect the estimate of collision likelihood compared to ECOB which uses densities of objects from MASTER. Nevertheless, at lower altitudes both metrics show a similar distribution of the values of normalised risk.

7. Conclusions

This work introduced new approaches to modelling future launch traffic and the risk associated with new missions. The launch traffic model is suitably flexible to capture various potential changes in this traffic over time while exploiting historical data to determine likely future patterns in launches. This model of future launch traffic is useful for simulating the future space environment and associated risk for missions. The risk model consists of metrics to quantify the induced and encountered risk of a mission that take into account the likelihood and severity of potential collisions. These metrics are fast to calculate for missions with one or many satellites such that the risk can be analysed over the mission's lifetime. The model used here to approximate the induced severity factor is very basic and its accuracy could be improved to give more realistic estimates of the consequences of a collision. For example, additional terms to account for the physics of fragment cloud dispersions that do not only consider altitude could improve the estimate of collision likelihood with these clouds. In addition, due to the scaling by number of objects, the collision likelihood and risk metrics occupy a large range of values that can be difficult to compare across scenarios and regimes. Further research is necessary to normalise these metrics such that the model output is more interpretable.

Declaration of Competing Interest

The authors declare that they have no known competing financial interests or personal relationships that could have appeared to influence the work reported in this paper.

Acknowledgments

This work was partially supported by the European Space Agency under the project "Dynamic Orbital Risk and Safety Assessments in a Changing Space Debris Envi-

ronment" (Contract Number: AO/1–11137/22/D/KS). The authors would like to thank Dr. Francesca Letizia for her advice and support with using the ECOB debris index.

References

Alfano, S., 2013. Determining a probability-based distance threshold for conjunction screening. J. Spacecr. Rock. 50 (3), 686–690. https://doi.org/10.2514/1.A32272.

Alfano, S., Oltrogge, D., 2018. Probability of collision: valuation, variability, visualization, and validity. Acta Astronaut. 148, 301–316. https://doi.org/10.1016/j.actaastro.2018.04.023.

Braun, V., Horstmann, A., Lemmens, S., et al., 2021. Recent developments in space debris environment modelling, verification and validation with MASTER. In: 8th European Conference on Space Debris. Darmstadt, Germany.

Diserens, S.D., Lewis, H.G., Fliege, J., 2020. NewSpace and its implications for space debris models. J. Space Saf. Eng. 7 (4), 502–509. https://doi.org/10.1016/j.jsse.2020.07.027.

Dolado-Perez, J., Di Constanzo, R., Revelin, B., 2013. Introducing medee - a new orbital debris evolutionary model. In: Proc. 6th European Conference on Space Debris, p. 8.

ESA Space Debris Office (2025). ESA's Annual Space Environment Report. LOG GEN-DB-LOG-00288-OPS-SD European Space Agency.

Horstmann, A., Manis, A., Braun, V., et al., 2021. Flux comparison of Master-8 and Ordem 3.1 modelled space debris population. In: Proc. 8th European Conference on Space Debris (virtual). Darmstadt, Germany, p. 9.

Horwood, J.T., Aristoff, J.M., Singh, N. et al. (2014). A comparative study of new non-linear uncertainty propagation methods for space surveillance. In Signal and Data Processing of Small Targets 2014 (pp. 135–158). SPIE volume 9092. doi:10.1117/12.2051353.

Johnson, N.L., Krisko, P.H., Liou, J.C., et al., 2001. NASA's new breakup model of evolve 4.0. Adv. Space Res. 28 (9), 1377–1384. https://doi.org/10.1016/S0273-1177(01)00423-9.

Kawamoto, S., Hirai, T., Kitajima, S., et al., 2018. Evaluation of space debris mitigation measures using a debris evolutionary model. Trans. Japan Soc. Aeronaut. Space Sci., Aerospace Technol. Japan 16 (7), 599–603. https://doi.org/10.2322/tastj.16.599.

Letizia, F., Colombo, C., Lewis, H.G., et al., 2017. Extending the ECOB space debris index with fragmentation risk estimation. In: 7th European Conference on Space Debris.

Lewis, H.G., Schwarz, B., George, S., et al., 2014. An assessment of CubeSat collision risk. In: 65th International Astronautical Congress. Toronto, Canada.

Liou, J.C., Hall, D.T., Krisko, P.H., et al., 2004. LEGEND – a three-dimensional LEO-to-GEO debris evolutionary model. Adv. Space Res. 34 (5), 981–986. https://doi.org/10.1016/j.asr.2003.02.027.

Liou, J.C., Kessler, D.J., Matney, M., et al., 2003. A new approach to evaluate collision probabilities among asteroids, comets, and Kuiper belt objects. In: Lunar and Planetary Science Conference, p. 1828.

Long, G., 2020. The impacts of large constellations of satellites. Technical Report The MITRE Corporation.

Lucken, R., Giolito, D., 2019. Collision risk prediction for constellation design. Acta Astronaut. 161, 492–501. https://doi.org/10.1016/j.actaastro.2019.04.003.

Martin, C., Walker, R., Klinkrad, H., 2004. The sensitivity of the ESA DELTA model. Adv. Space Res. 34 (5), 969–974. https://doi.org/10.1016/j.asr.2003.02.028.

Matney, M., Manis, A., Anz-Meador, P., et al., 2019. The NASA orbital debris engineering model 3.1: development, verification, and validation. In: In International Orbital Debris Conference (IOC). Sugar Land, TX.

McKnight, D., Witner, R., Letizia, F., et al., 2021. Identifying the 50 statistically-most-concerning derelict objects in LEO. Acta Astronaut. 181, 282–291. https://doi.org/10.1016/j.actaastro.2021.01.021.

McNally, K., Mecinas, F.J.S., Johnson, B., et al., 2024. Dynamic orbital risk assessment in a changing space debris environment. In: 75th International Astronautical Congress. Milan, Italy, pp. 1398–1411.

Naaman, M., 2021. On the tight constant in the multivariate Dvoretzky–Kiefer–Wolfowitz inequality. Stat. Probabil. Lett. 173, 109088. https://doi.org/10.1016/j.spl.2021.109088.

Narumi, T., Hanada, T., Kawamoto, S., 2008. Space debris environmental evolutionary model in low earth orbit. Space Technol. Japan, Japan Soc. Aeronaut. Space Sci. 7, 11–17. https://doi.org/10.2322/stj.7.11.

Radtke, J., Stoll, E., Lewis, H., et al., 2017. The impact of the increase in small satellite launch traffic on the long-term evolution of the space debris environment. In: Flohrer, T., Schmitz, F. (Eds.), 7th European Conference on Space Debris. The European Space Agency (ESA), Darmstadt, Germany.

Rao, A., Letizia, F., 2021. An Integrated Debris Environment Assessment Model. In Proc. 8th European Conference on Space Debris (virtual). ESA Space Debris Office, Darmstadt, Germany.

Ryan, S., Christiansen, E.L., 2010. Micrometeoroid and orbital debris (MMOD) shield ballistic limit analysis program. Technical Report Johnson Space Center.

Stein, L. (2022). LEO SATCOM Report. URL: https://www.primemoverslab.com/resources/ideas/leo-satcom.pdf.

Uriot, T., Izzo, D., Simões, L.F., et al., 2022. Spacecraft collision avoidance challenge: Design and results of a machine learning competition. Astrodynamics 6 (2), 121–140. https://doi.org/10.1007/s42064-021-0101-5.

Virgili, B.B., 2016. DELTA (Debris Environment Long Term Analysis). In: In 6th International Conference on Astrodynamics Tools and Techniques (ICATT), p. 8.

Wang, X.-W., Liu, J., 2019. An introduction to a new space debris evolution model: SOLEM. Adv. Astron. 2019, 1–11. https://doi.org/10.1155/2019/2738276.

Wilson, C., Vasile, M., Feng, J., et al., 2024. Modelling Future Launch Traffic and its Effect on the LEO Operational Environment. In: In AIAA SCITECH 2024 Forum. American Institute of Aeronautics and Astronautics, Orlando, FL, p. 1814.

Wizniowski, T., Rickman, H., 2013. Fast geometric method for calculating accurate minimum orbit intersection distances (MOIDs). Acta Astronom. 63, 293–307.

Woodburn, J., Coppola, V., Stoner, F., 2010. A description of filters for minimizing the time required for orbital conjunction computations. Adv. Astronaut. Sci. 135 (2), 1157–1173.